

**A DYNAMIC FINITE ELEMENT FRAMEWORK BUILT TOWARDS THE INVERSE
PROBLEM OF SOFT TISSUES**

By

MEGAN L. KOGIT

A thesis submitted to the
Graduate School-New Brunswick
Rutgers, The State University of New Jersey
in partial fulfillment of the requirements

for the degree of

Master of Science

Graduate Program in Mechanical and Aerospace Engineering

written under the direction of

Dr. Assimina A. Pelegri

and approved by

New Brunswick, New Jersey

January 2008

ABSTRACT OF THE THESIS

A DYNAMIC FINITE ELEMENT FRAMEWORK BUILT TOWARDS THE INVERSE PROBLEM OF SOFT TISSUES

by MEGAN L. KOGIT

Thesis Director:

Dr. Assimina A. Pelegri

This study seeks to simulate soft tissue behavior with a custom finite element analysis. It is the eventual goal of this team to explore the inverse problem of soft tissues, and this simulation study will play an integral role in that process. It is hoped that new information regarding the elastic properties of soft tissue can be used to diagnose disease processes and improve health care delivery.

In this investigation, soft tissue is modeled as a linear, isotropic, elastic, and nearly incompressible material. A dynamic finite element problem was defined consistent with the experimental protocol of harmonic motion imaging, an elasticity imaging technique that utilizes acoustic radiation force to induce localized displacements within soft tissue samples.

The finite element equations of motion in this investigation were solved using the Newmark method, an approach commonly used by engineers to determine the dynamic response of structures under the action of any general time-dependent loads. It was found that the displacement results obtained with the Newmark method made physical sense and agreed with the observations of other researchers in this field, suggesting that the current finite element analysis is a suitable simulation of soft tissue behavior.

Acknowledgements

I would first like to thank my advisor, Dr. Assimina Pelegri. Her light spirit and support definitely made my research experience a pleasant one. Dr. Baoxiang Shan has also been invaluable during this research. His expertise helped me every step of the way. I am also thankful to Dr. Ellis Dill and Dr. Noshir Langrana, my defense committee members, for taking the time to read my thesis and helping me with this degree. I am additionally thankful to Dr. Dill for all his tutoring in the past. He has been an integral part in my progress as a researcher and as a student.

I would also like to thank the MAE faculty for providing me with excellent teaching and heart-felt guidance throughout all my years at Rutgers. I would especially like to thank the MAE department administrators and my advisor for the fellowship support of my graduate studies; it would have been hard at times without it.

I would also like to thank my parents, Vickie and Tim Kogit, who always taught me that an education means everything. My sister, Wynter, and her husband, Keith, helped me equally as much along the way, providing me with a home away from home during the long months away at school.

And last I leave James, my rock, without whom I would be lost.

Table of Contents

Abstract	ii
Acknowledgements	iii
List of Tables	vi
List of Figures	viii
1. Introduction	1
1.1. Problem Statement	1
1.2. Motivation	2
1.3. Current State of the Art	4
1.4. Relevant Work	5
1.5. Outline	7
2. Formulation of the Finite Element Method	9
2.1. Basic Equations of Linear Elasticity.....	9
2.2. Finite Element Framework	10
2.3. Principle of Virtual Work	12
2.4. Finite Element Equations of Linear Elasticity	14
2.5. Provisions for Nearly Incompressible Materials	17
2.5.1. Principle of Virtual Work – Revisited	17
2.5.2. The Revised Finite Element Equations	19
3. Static Analysis	24
3.1. Source Code	24
3.1.1. Model Parameters	24
3.1.2. Validating the Local Stiffness Matrix	27
3.1.3. Validating the Global Stiffness Matrix	31

3.2. Source Code Alterations	33
3.2.1. Model Parameters	34
3.2.2. Validating the Altered Local Stiffness Matrix	35
4. Dynamic Analysis	37
4.1. Finite Element Equations of Motion	37
4.1.1. Mass Matrix	38
4.1.2. Force Vector	40
4.1.3. Model Parameters for Dynamic Analysis	43
4.2. Newmark Method	44
4.2.1. Newmark Method Parameters	47
4.2.2. Starting Conditions	52
4.2.3. Programming Assessment	52
5. Dynamic Analysis Results	55
5.1. Physical Observations	55
5.1.1. Massless System Response	55
5.1.2. Effect of Young's Modulus	57
5.2. Multi-Frequency Forcing Function	59
5.3. Short-cut Method	64
6. The Inverse Problem – A Current Concern	69
6.1. Methodology	69
6.2. Principle of Superposition	72
6.3. Proposed Routine	74
7. Conclusions	77
8. Future Work	82
Appendix	84
References	87

List of Tables

2.1	The basic equations of linear elasticity used in the current formulation of the finite element method to model soft tissue. The assumptions of material isotropy and isothermal deformation were also made.	9
3.1	Specifications used to construct a compressible finite element model with the original source code. The original source code could not handle the case of material incompressibility, so for an initial gauge of its accuracy, the code was tested as downloaded for a compressible model of soft tissue.	25
3.2	ANSYS specifications used to construct the compressible material model identified in Table 3.1.	27
3.3	ANSYS specifications used to construct an incompressible material element. A model of this type in ANSYS was needed to assess the accuracy of the programming modifications added to the original source code to handle the case of material incompressibility.	34
4.1	Model parameters used in the current dynamic simulation of soft tissue. The material constants used to define the mass and incompressible stiffness matrices are shown, as well as the parameters used to define the forcing function $F_o(t)$.	43
4.2	Parameters used during the current dynamic finite element analysis of a soft tissue model with the Newmark method. Time step h and the time for analysis t cannot be arbitrarily assigned; convergence analyses were performed for N and PER to assess the optimal values of these parameters, respectively.	47
4.3	Parameters used to set up a transient dynamic analysis in ANSYS, which was used to assess the performance of the dynamic analysis performed with the current MATLAB simulation using the Newmark method.	53

5.1	Multi-frequency force versus single-frequency force results. Each force case is in a separate column, and the displacement amplitudes for each particular frequency of interest are compared. This was done to assess the efficacy of the Newmark method in handling more than one frequency component in its excitation force.	63
5.2	A comparison of the short-cut and Newmark methods, where displacement amplitudes are displayed for several nodes and excitation frequencies acquired with both methods. The short-cut method was employed as a rough estimate of the accuracy of the Newmark method.	66
5.3	A list of the model's natural frequencies in proximity to the excitation frequencies used.	68
6.1	A comparison of the stiffness matrix entries collected from the original stiffness matrix versus that computed from the short-cut method (Eqn (6.1)).	71

List of Figures

2.1	An 8-node, 3D quadrilateral element labeled with global x - y - z and local ξ - η - ζ coordinate systems. A global coordinate system is used for the whole model (multiple elements) while a local coordinate system is used for each particular element. The size of the model is also indicated with the length of its edges, denoted by 'a', 'b', and 'c'.	11
2.2	The eight node brick element used in the current investigation has one pressure node at its center, indicating that pressure is treated as a constant within each element of the model. Element pressure needs to be considered as part of the analysis for incompressible materials.	20
3.1	An illustration of the reduction of the global stiffness matrix. Since the surface $z = 0$ of the model was fixed, the displacement at each node on that surface was known to be zero and could be removed from the displacement vector. The corresponding rows and columns of the stiffness matrix had to be removed as well because of linear algebra, thereby reducing the size of the problem.	26
3.2	General architecture of the original source code. First the local stiffness matrix was constructed from material properties and shape functions, and was then assembled into the global stiffness matrix. The static problem could then be solved using the boundary and support conditions.	28
3.3	8-node brick elements used in MATLAB and ANSYS. Each element is labeled with a global coordinate system and node numbering scheme unique to the program it was constructed in.	28
3.4	An illustration of the scheme used to view the local stiffness matrix constructed in ANSYS. Since the stiffness matrix is not a variable for viewing in ANSYS, this scheme was devised using operations and variables possible in the program. This was needed to assess the validity of the local stiffness matrix constructed with the original source code.	29

3.5	Displacement equivalencies between MATLAB (left) and ANSYS (right). Since the orientation of the global coordinate systems and the node numbering schemes for each element are different in MATLAB and ANSYS, the displacement at one node in one direction in MATLAB is equivalent to the displacement at a node with another number in another direction in ANSYS.	30
3.6	The reaction forces of ANSYS versus the corresponding column of the local compressible stiffness matrix from the MATLAB source code. Each row of the stiffness “column” is denoted by the corresponding row entry of the displacement and force vectors. The displacement equivalencies discussed in Figure (3.5) apply to forces as well and aid in the comparison.	31
3.7	10x10x10 element models used in MATLAB and ANSYS. Each model is labeled with its global coordinate system unique to the program it was constructed in. A force was applied at the geometrically central node which, for a 4mm mesh, translates to coordinate (20,20,20)mm. The force was applied towards the fixed surface at $z = 0$ (in the negative z -direction).	32
3.8	The reaction forces of ANSYS versus the corresponding column of the local incompressible stiffness matrix from the MATLAB source code. Each row of the stiffness “column” is denoted by the corresponding row entry of the displacement and force vectors. The displacement equivalencies discussed in Figure (3.5) apply to forces as well and aid in the comparison.	36
4.1	The lumped mass approach used to formulate the mass matrix in the current simulation, where the mass of each element is assumed to reside at its nodes. ‘a’ and ‘b’ denote the edge lengths of each element, and ρ is the material density. Depending upon location, the mass at each node will vary accordingly, and is some factor of $m = \rho ab$.	39
4.2	A schematic of harmonic motion imaging. A focused ultrasound (FUS) transducer of intensity $I(t)$ operating at a frequency f excites a small volume of tissue (V), with an acoustic absorption coefficient α dependent upon frequency f . Sound travels in the tissue at speed c . An acoustic radiation force $F_o(t)$ is generated in the tissue, which oscillates at frequency f_{req} . A diagnostic ultrasound transducer monitors the resulting tissue oscillations.	

.....	41
4.3 Multiple equilibrium configurations of HMI. During experimentation, the acoustic radiation force (i.e., the forcing function $F_o(t)$ in FEM) can only be applied to one point at a time. In the current finite element simulation, this necessitates a unique force vector $\mathbf{F}(t)$ and a unique set of equilibrium equations for each point scanned.	42
4.4 Convergence analysis with N sampling points per loading period. The amplitude of the displacement at a particular point in time was plotted as a function of N to help define the appropriate time step h for the Newmark method.	49
4.5 A 2D slice of the finite element model with the forcing function $F_o(t)$ applied to the geometrically central node with coordinates (20,20,20)mm. $F_o(t)$ acts in the negative z -direction towards the fixed surface at $z = 0$.	50
4.6 The forcing function $F_o(t)$ applied to the model is a harmonic force that is zero at time $t = 0$ oscillating about a mean of 0.01N with an amplitude of 0.01N. The values of the nonzero mean and amplitude were determined using parameters appropriately defined in Table (4.1) from references [5,8,12,13,18,19].	50
4.7 Convergence analysis with PER loading periods. The amplitude of the displacement with $N = 30$ samples per loading period was plotted as a function of PER to help determine a sufficient length of time t required for dynamic analysis with the Newmark method.	51
4.8 The dynamic z -displacement ('UZ') recorded at the point of loading from both MATLAB (—) and ANSYS (— • —) simulations.	54
5.1 A one-dimensional massless elastic system, represented by a simple elastic spring with spring constant k . This figure helps visualize that if the mass in the current finite element simulation was neglected, the model would respond instantaneously to applied force regardless of material stiffness.	56

5.2	The dynamic z-displacement ('UZ') recorded at the point of loading in the current MATLAB simulation for the (massless) tissue model. Three different cases of material stiffness are shown, where Young's modulus E equals 20kPa (—), 50kPa (- · -), and 80kPa (······). The forcing function $F_o(t)$ (— · —) is also depicted. A time shift is also labeled between the displacement responses and the forcing function $F_o(t)$.	56
5.3	Dynamic response of the current tissue model (with mass). Two different cases of material stiffness are shown, where Young's modulus E equals 20kPa (—) and 50kPa (— ·). The initial time shift introduced by the Newmark method/ starting conditions is also labeled.	57
5.4	A plot of displacement amplitude versus Young's modulus, with values ranging between 20 – 60kPa. Displacement amplitude decreases with material stiffness.	58
5.5	A one-dimensional elastic system, shown as a simple elastic spring with a mass on the end. This figure helps visualize that if the material of the current soft tissue model was made stiffer (i.e., the Young's modulus was increased), the material would respond quicker to applied load. This decrease in response time would be evident in the displacement response.	59
5.6	100Hz excitation frequency case. $F_o(t)$, as it was applied in the (negative) z-direction at the point of loading is shown in the top graph, and the resulting z-displacement at that point is shown in the second graph. The bottom graph displays the frequency spectrum of the displacement response.	60
5.7	200Hz excitation frequency case. Reference the caption of Figure (5.6) for a more thorough description.	61
5.8	Case where the forcing function $F_o(t)$ was composed of four frequency components; 50, 100, 200, and 400Hz. Reference the caption of Figure (5.6) for a more thorough description.	62

5.9	A 2D slice of the model indicating the nodes listed in Table (5.2). All nodes lie along the z -direction in the center of the model.	66
6.1	An illustration of the linear algebra employed for the multiplication of the stiffness matrix and the displacement vector to determine each value in the force vector.	70
6.2	An illustration of the principle of superposition, used in the proposed inverse routine. This principle helps determine the displacement at nodes adjacent to the one under loading in a single equilibrium configuration.	72
6.3	An illustration of the principle of superposition, used in the proposed inverse routine. As opposed to Figure (6.2), the adjacent node of interest is now above the node being loaded.	74
6.4	An illustration of the force and displacement vectors for a given equilibrium configuration of HMI with two additional values filled in by using the principle of superposition.	75
6.5	The general procedure of the proposed inverse routine.	76

Chapter 1

Introduction

1.1 Problem Statement

From repeated clinical observations, the tactile characteristics of tumors are known to differ from those of normal surrounding tissues. This accounts for the widespread use of palpatory exams to screen for cancer in accessible regions of the body, such as the breast and prostate.

Physicians use palpation to qualitatively assess the stiffness parameters of tissue for a rough diagnosis. These stiffness parameters relate to physical properties called elastic moduli, which quantify a tissue's resistance to deformation. It is an accepted fact that these elastic moduli vary between tissue types. This has motivated the development of many methods to investigate the mechanical properties of tissues. These methods are collectively known as "elasticity imaging" techniques. It is hoped that elasticity imaging techniques will yield new information about tissues that could be used to diagnose disease processes, as well as provide insight to the development of surgical simulators and biomechanical devices.

There is a wide spectrum of elasticity imaging techniques. Some researchers perform mechanical compression tests on soft tissue specimens to determine Young's modulus in a specified strain range. Still others are developing methods to perturb soft tissue remotely with acoustic radiation force. In some instances, acoustic radiation force can be viewed as a "point-like" force, which is capable of inducing localized displacements within a tissue sample. These localized displacements can be used to qualitatively infer the relative stiffness distribution in the medium.

Finite element modeling (FEM) can be used as a suitable computational analog to experimental methods using point-like acoustic radiation force; the localized displacements obtained experimentally can be likened to nodal displacements in FEM. These nodal displacements are determined through a “forward” finite element analysis, where the material properties and loading conditions for a given solid mechanics model must be specified. In the study of soft tissues, however, localized displacements are measured experimentally and the loading conditions are essentially known; it is the material properties that must be determined. This is an example of a classic inverse problem.

The inverse problem cannot be solved with any commercial finite element package; these packages are built for forward analysis, only. Thus, it is the mission of this research team to develop the custom software needed to provide this type of inverse analysis.

This thesis documents the team’s progress in developing a custom dynamic (forward) finite element analysis on a soft tissue model. The assumptions used are that for a linear, isotropic, elastic, and incompressible material. This forward analysis is necessary to generate simulation data on which to test an inverse procedure. The team’s approach to addressing the inverse problem is a work-in-progress, and is discussed at the end of this thesis along with some preliminary results. Ideally, the inverse routine’s eventual implementation into an experimental system will enable this team to determine the mechanical properties of soft tissue for the betterment of medical diagnosis and design.

1.2 Motivation

Breast cancer is the most commonly diagnosed form of cancer in women in the United States. According to statistics from the American Cancer Society for 2007, women in the United States

have a one in eight lifetime risk of developing breast cancer [1]. It is the second leading cause of cancer deaths in women, second only to cancers of the lung and bronchus [2].

At this time, there is no guaranteed way to prevent breast cancer from developing [1]. However, numerous studies have shown that early detection saves lives and increases treatment options. In the case of breast cancer, the American Cancer Society's guidelines for early detection vary depending upon on a woman's age, and include mammography and clinical breast examinations (CBEs). For high risk women, magnetic resonance imaging (MRI) is also recommended [1].

Mammography and MRI image tissue properties that are generally unrelated to the distinct hardness of pathological tissue, as detected by palpation [3]. However, palpation during CBEs is not very effective when lesions are small and/or deep beneath the skin. Improving upon the effectiveness of CBEs, elasticity imaging techniques seek to quantify the elastic contrast that has been qualitatively observed between normal, soft tissue and hard, cancerous nodules during palpation.

In the doctoral research of Ladeji-Osias [4], performed under the direction of Dr. Noshir Langrana, single and multi-probe indentation tests were performed on commercial breast models and cadaveric specimens to investigate the biomechanics of palpation. The shortcomings of manual palpation (i.e., its inability to detect small and/or deep lesions) were observed in their mechanical testing as well.

1.3 Current State of the Art

There is a wide spectrum of approaches used to explore the mechanical properties and behavior of tissues, all with the purpose of advancing health care delivery. These approaches are collectively known as elasticity imaging techniques.

One such approach to elasticity imaging involves mechanical compression tests. Krouskop et al. [5] used a commercial materials testing system (Instron, Inc., Canton, MA) to subject breast and prostate tissue samples to compression loading. Other research groups, such as Wellman et al. [6] and Egorov et al. [7], constructed their own, portable indentation devices that could be used in the operating room immediately after excision. But regardless of the device used, and without refute, mechanical compression tests have shown that different tissue and cancer types exhibit different mechanical behaviors and elastic moduli.

Aside from mechanical compression tests, other elasticity imaging methods can provide an actual “image” of internal tissue displacement under applied load. This displacement distribution qualitatively relates to the relative stiffness distribution within the tissue. Some of these methods, such as harmonic motion imaging (HMI), use acoustic radiation force generated inside tissue as a remote, dynamic mechanical stimulus.

Harmonic motion imaging (HMI) [8-12] is an elasticity imaging technique that uses acoustic radiation force to induce oscillatory displacements at the focus of a focused ultrasound (FUS) transducer for the detection of localized stiffness changes. Since the focal volume of a focused transducer is usually small (on the order of mm^3 [13]), the acoustic radiation force generated within the volume can be thought of as a point-like load applied to the tissue. The displacement induced in the tissue by this load is estimated in the direction of loading by a diagnostic

ultrasound transducer aligned directly with the focus of the FUS transducer. With this set-up, only one “point” in one direction can be loaded, and the corresponding displacement at that point only and in that direction only is monitored simultaneously.

The transducer set-up can be shifted along a 2D x - y grid using a computer-controlled positioning system so that displacement measurements can be obtained for various points in a plane. Typically, the step size of such a computer-controlled positioning system is on the order of millimeters [9,11,12]. To obtain data for multiple planes, the depth of the tissue probed by the focus of the FUS transducer can be adjusted by repositioning the transducer set-up in the z -direction. The displacement signal acquired at each point is then filtered to yield the amplitude of the displacement at the excitation frequency; all other frequencies in the response are disregarded. These amplitudes are then used to construct a 2D image that is related to the relative stiffness distribution in that plane. If multiple planes are combined, the stiffness distribution in the whole sample can be seen as a 3D image [9].

Mechanical compression tests and harmonic motion imaging are just two types of many elasticity imaging techniques. It is stressed that the methods discussed here are only a few of the many in existence. Only harmonic motion imaging (HMI) was discussed in detail because it is the most pertinent to this investigation.

1.4 Relevant Work

The current investigation is focused upon simulating the experimental method of harmonic motion imaging (HMI) with finite element analysis. Most recently in 2007, Maleke et al. [9] performed a simulation of harmonic motion imaging using COMSOL (Comsol MultiphysicsTM, Comsol Inc., Burlington, MA). They used a two-dimensional, linear, elastic, and nearly

incompressible ($\nu = 0.49$) model of soft tissue 35mm by 30mm in size with triangular elements. The Young's modulus was varied from 20 – 60kPa. The acoustic pressure field generated by an FUS transducer was simulated and applied as the source of excitation. It was found that the resulting displacement was localized and was greatest at the center of the pressure field, spanning approximately ± 3 mm laterally from the focal zone.

The inventors of HMI, Kullervo Hynynen and Elisa Konofagou [10], have performed their own finite element simulations using ALGOR (Algor, Inc., Pittsburg, PA). In a paper published in 2003 [8], they used finite element simulations of a linear, elastic, nearly incompressible ($\nu = 0.495$) soft tissue model to study the effect of parameters such as loading frequency and tissue modulus on the resulting displacement estimate. They used a two-dimensional model 40x40mm in size with triangular elements and a stiffness of 30kPa. An inclusion with a diameter of 6.6mm was placed in the center, and its stiffness was varied between 20kPa to 50kPa. The center node of the inclusion was loaded with a harmonic force oscillating about a positive mean with frequencies ranging from 200Hz to 800Hz. Only the oscillation at the excitation frequency was considered; a low frequency component observed in each response was removed through high-pass filtering to preserve the consistency between simulations and experiments (where only the higher, excitation frequency was tracked).

When the force was applied directly to the center of the inclusion, a decrease of the displacement amplitude with inclusion stiffness was observed at all frequencies investigated. A small upshift in the frequency of the oscillatory displacement signal (on the order of tens of Hz) was also observed with increasing stiffness. Lastly, for a given inclusion stiffness, a larger displacement amplitude was observed at smaller frequencies.

Aside from HMI, Konofagou and Hynynen, in addition to Jonathan Thierman, performed a finite element simulation study of ablation with ultrasound-stimulated acoustic emission imaging (USAE) in 2001 [14]. USAE is very similar to HMI, where the only marked difference is the method of displacement detection; HMI uses ultrasound, while USAE uses an external hydrophone [8]. However, this difference did not affect the gist of their finite element simulations in relation to the current investigation. In ALGOR simulations comparable to those performed in 2003, the group examined the displacement amplitude as a function of excitation frequency for several inclusion-to-background stiffness ratios. They observed the general trend that over a range of 0 to 50kHz, the displacement amplitude decreased with excitation frequency. On the small scale, though, the amplitude values oscillated wildly and unpredictably in the range of excitation frequencies between 0 to 12kHz.

The simulations discussed previously were performed with commercial finite element packages (COMSOL and ALGOR), so while the basis of those simulations is comparable to the current investigation, the intent is much different. The current simulation was built from the bottom up in MATLAB (The MathWorks Inc., Natick, MA) with the intent that an inverse routine could eventually be integrated seamlessly; the simulation data and inverse solution would all be available from the same program. With commercial finite element packages, an inverse routine cannot be integrated and must be performed separately. This is what sets this research and the current simulation apart from the others.

1.5 Outline

Chapter 1 of this thesis provides the reader with the background needed to understand the motivation of the current research. The current state of technology in relation to this research is also discussed, as are other soft tissue simulations similar to work presented here.

Chapter 2 details the formulation of the finite element method used in the current investigation from the basic equations of linear elasticity to approximate the behavior of soft tissue, while also addressing the provisions required for nearly incompressible materials.

Chapter 3 discusses the basic architecture of the current finite element simulation, and that this source code was originally capable of solving the static problem for compressible material models, only. This chapter also documents the team's efforts in investigating the trustworthiness of the source code and the subsequent alterations for material incompressibility by comparing its results to that of a commercial finite element package.

Chapter 4 discusses how the static problem of the previous chapter evolved into a dynamic problem with the definition of a time-varying force vector. The subsequent equations of motion were solved using the Newmark method, a popular approach with engineers to determine the dynamic response of structures under any general time-dependent loads.

Chapter 5 examines the dynamic results obtained with the current analysis to determine its efficacy in simulating soft tissue behavior. The Newmark method was also compared to a "short-cut" method as a rough measure of solution accuracy.

Chapter 6 provides insight into the inverse problem at hand, addressing what some other groups in the field have done thus far. While it is mainly a work-in-progress, the inverse routine proposed is discussed and some preliminary results are presented.

Chapter 7 discusses the conclusions drawn from the current research, while Chapter 8 suggests topics for future work.

Chapter 2

Formulation of the Finite Element Method

2.1 Basic Equations of Linear Elasticity

For small deformations, it can be assumed that soft tissue behaves as a linear solid [15]. This is the basic assumption used in the subsequent formulation of the finite element method, which will be based upon the basic equations of linear elasticity. The basic equations of linear elasticity are a set of differential equations governing the motion of infinitesimal, linearly elastic material volumes experiencing small deformations. A further assumption of material isotropy will also be made, although this property is generally not observed experimentally. The basic equations of linear elasticity with the assumption of material isotropy are listed in Table (2.1) below and are described hereafter.

Equations	Description	Additional Information	Equation Number
$\frac{\partial \tau_{ij}}{\partial x_j} + \bar{b}_i = 0$	Balance of Momentum	$\bar{b}_i = b_i - \rho \ddot{u}_i$	(2.1)
$\varepsilon_{ij} = \frac{1}{2} \left(\frac{\partial u_i}{\partial x_j} + \frac{\partial u_j}{\partial x_i} \right)$	Geometric Equations	-	(2.2)
$T_i = T_i^o$	Boundary Conditions	$T_i = \tau_{ij} n_j$	(2.3)
$u_i = u_i^o$	Support Conditions	-	(2.4)
$\tau_{ij} = 2\mu \varepsilon_{ij} + \lambda \varepsilon_{kk} \delta_{ij}$	Constitutive Relations	$\mu = G = \frac{E}{2(1+\nu)} ; \quad \lambda = \frac{2\mu\nu}{1-2\nu}$	(2.5)

Table 2.1

The basic equations of linear elasticity used in the current formulation of the finite element method to model soft tissue. The assumptions of material isotropy and isothermal deformation were also made.

In Eqn (2.1) – Eqn (2.5), the subscripts i and j indicate Cartesian coordinate direction and surface, respectively. In the balance of momentum equations (Eqn (2.1)), $\boldsymbol{\tau}$ is the symmetric stress tensor acting on each surface of the volume, b_i is the body force, ρ is material density, and \ddot{u}_i is the second time derivative of the displacement vector. The geometric relations (Eqn (2.2)) relate the strain tensor $\boldsymbol{\varepsilon}$ to the displacement vector \mathbf{u} and coordinate direction x . In Eqn (2.3), T_i is the force per unit surface area (traction) in each direction i , where n_j is the unit vector normal to each surface. Traction T_i and the displacement vector \mathbf{u} can be constrained on each surface of the material volume, and are thus called the boundary (Eqn (2.3)) and support conditions (Eqn (2.4)), respectively. The constitutive relations (Eqn (2.5)) relate the stress tensor $\boldsymbol{\tau}$ to the strain tensor $\boldsymbol{\varepsilon}$ for an isotropic material experiencing isothermal deformation. δ is the Kronecker delta, and μ and λ are the shear modulus and 1st Lamé constant, respectively. E is Young's modulus, and ν is Poisson's ratio.

2.2 Finite Element Framework

An approximate solution to the set of differential equations Eqn (2.1) – Eqn (2.5) can be achieved by using a numerical method known as the finite element method. The fundamental idea is to divide a material body into a series of small subsections called *elements*. Under applied loading, the object's deformation (i.e., continuous displacement field) can be approximated in each element by interpolating between the values of the displacement at specific points on each element called *nodes*. These discrete *nodal displacements* are determined via finite element analysis; they are a necessary ingredient to approximating the material's displacement field, the solution to the elasticity problem.

To construct the finite element framework, first define \mathbf{D} , a vector of all the displacements at each node for a single element, such that

$$\mathbf{D} = \begin{bmatrix} U_1 \\ V_1 \\ W_1 \\ U_2 \\ \vdots \\ W_N \end{bmatrix} \quad (2.6)$$

where, in Cartesian coordinates, U , V , and W are the x -, y -, and z - displacements at nodes 1, 2, ..., N . To attain the displacement field within the element, *shape functions* must be used to interpolate inside the body based on the nodal displacement values. For an 8-node three-dimensional (3D) quadrilateral, linear shape functions are of the form:

$$N_k = \frac{1}{8}(1 + \xi_k \xi)(1 + \eta_k \eta)(1 + \zeta_k \zeta), \quad (2.7)$$

where ξ - η - ζ comprise the local coordinate system of the element, originating at its center. $-1 \leq \xi \leq 1$, and the same is true for η and ζ . ξ_k , η_k , and ζ_k are the values of ξ , η , and ζ (either ± 1) of the k^{th} (1, 2, ..., 8) node. Illustrated below in Figure 2.1 is a single element labeled with both x - y - z and ξ - η - ζ coordinate systems with nodes 1 through 8.

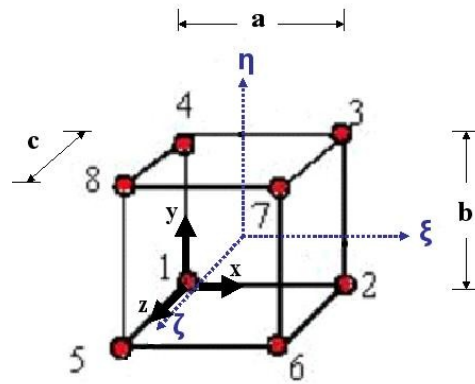


Figure 2.1

An 8-node, 3D quadrilateral element labeled with global x - y - z and local ξ - η - ζ coordinate systems. A global coordinate system is used for the whole model (multiple elements) while a local coordinate system is used for each particular element. The size of the model is also indicated with the length of its edges, denoted by 'a', 'b', and 'c'.

The displacement field in the element can be approximated by

$$u = \sum_{k=1}^N N_k U_k, \quad v = \sum_{k=1}^N N_k V_k, \quad w = \sum_{k=1}^N N_k W_k \quad (2.8)$$

where u , v , and w represent the displacement field in the x , y , and z directions at any given ξ - η - ζ coordinate in the volume. In matrix form, the displacement field may be written as

$$\mathbf{u} = \mathbf{N}\mathbf{D}, \quad (2.9)$$

where

$$\mathbf{u} = \begin{bmatrix} u \\ v \\ w \end{bmatrix} \quad (2.10)$$

and

$$\mathbf{N} = \begin{bmatrix} N_1 & 0 & 0 & N_2 & 0 & 0 & \cdots \\ 0 & N_1 & 0 & 0 & N_2 & 0 & \cdots \\ 0 & 0 & N_1 & 0 & 0 & N_2 & \cdots \end{bmatrix} \quad (2.11)$$

where N_1 is the shape function at node 1 of the element, and so forth.

2.3 Principle of Virtual Work

The principle of virtual work may be used to establish the fundamental equations of the finite element methodology. To derive the virtual work theorem, multiply the momentum equation

(Eqn (2.1)) by an arbitrary function \bar{u}_i :

$$\frac{\partial \tau_{ij}}{\partial x_j} \bar{u}_i + b_i \bar{u}_i - \rho \ddot{u}_i \bar{u}_i = 0 \quad (2.12)$$

Define another function $\bar{\varepsilon}_{ij}$ such that

$$\bar{\varepsilon}_{ij} = \frac{1}{2} \left(\frac{\partial \bar{u}_i}{\partial x_j} + \frac{\partial \bar{u}_j}{\partial x_i} \right). \quad (2.13)$$

Since the stress tensor $\boldsymbol{\tau}$ is symmetric ($\tau_{ij} = \tau_{ji}$),

$$\tau_{ij} \bar{\varepsilon}_{ij} = \frac{1}{2} \tau_{ij} \frac{\partial \bar{u}_i}{\partial x_j} + \frac{1}{2} \tau_{ij} \frac{\partial \bar{u}_j}{\partial x_i} = \tau_{ij} \frac{\partial \bar{u}_i}{\partial x_j} \quad (2.14)$$

if the indices $i \rightarrow j$ and $j \rightarrow i$ in the second term between the equal signs.

By taking the volume integral of Eqn (2.12) and using integration by parts on the first term, Eqn (2.15) below results:

$$\int_V \frac{\partial}{\partial x_j} (\tau_{ij} \bar{u}_i) dV - \int_V \tau_{ij} \bar{\varepsilon}_{ij} dV + \int_V (b_i - \rho \ddot{u}_i) \bar{u}_i dV = 0 \quad (2.15)$$

Eqn (2.15) could be further modified by applying Gauss' theorem on the transformation of integrals, stated below:

$$\int_V \frac{\partial f_j}{\partial x_j} dV = \int_S n_j f_j dA \quad (2.16)$$

where $f_j = \tau_{ij} \bar{u}_i$ in this case. By applying Gauss' theorem to the integral in Eqn (2.15), the final resulting integral is:

$$\int_S T_i \bar{u}_i dA + \int_V (b_i - \rho \ddot{u}_i) \bar{u}_i dV = \int_V \tau_{ij} \bar{\varepsilon}_{ij} dV \quad (2.17)$$

where $T_i = \tau_{ij} n_j$ are the surface tractions as defined in Eqn (2.3). This is the basic virtual work theorem of linear elasticity if \bar{u}_i and $\bar{\varepsilon}_{ij}$ represent virtual variations in displacement and strain, respectively, for the material volume. The left-hand side of Eqn (2.17) represents the work done by external loads (surface tractions, body and inertial forces) and the right-hand side represents the work done by internal stresses τ_{ij} .

2.4 Finite Element Equations of Linear Elasticity

When applied to the assembly of finite elements, the virtual work formula in Eqn (2.17) for the whole material body becomes

$$\sum_{m=1}^M \int_{S_m} \bar{\mathbf{u}}^T \mathbf{T} dA + \sum_{m=1}^M \int_{V_m} \bar{\mathbf{u}}^T (\mathbf{b} - \rho \ddot{\mathbf{u}}) dV = \sum_{m=1}^M \int_{V_m} \bar{\boldsymbol{\varepsilon}}^T \boldsymbol{\tau} dV \quad (2.18)$$

for all elements $1 \dots M$. $\boldsymbol{\tau}$ is defined as

$$\boldsymbol{\tau}^T = [\tau_{11} \quad \tau_{22} \quad \tau_{33} \quad \tau_{12} \quad \tau_{23} \quad \tau_{31}], \quad (2.19)$$

such that the constitutive relations of Eqn (2.5) for an isotropic material can be written in matrix form as

$$\boldsymbol{\tau} = \mathbf{C} \boldsymbol{\varepsilon} \quad (2.20)$$

where \mathbf{C} is defined as:

$$\mathbf{C} = \begin{bmatrix} 2\mu + \lambda & \lambda & \lambda & 0 & 0 & 0 \\ \lambda & 2\mu + \lambda & \lambda & 0 & 0 & 0 \\ \lambda & \lambda & 2\mu + \lambda & 0 & 0 & 0 \\ 0 & 0 & 0 & \mu & 0 & 0 \\ 0 & 0 & 0 & 0 & \mu & 0 \\ 0 & 0 & 0 & 0 & 0 & \mu \end{bmatrix} \quad (2.21)$$

and

$$\boldsymbol{\varepsilon}^T = [\varepsilon_{11} \quad \varepsilon_{22} \quad \varepsilon_{33} \quad 2\varepsilon_{12} \quad 2\varepsilon_{23} \quad 2\varepsilon_{31}] \quad (2.22)$$

The strain vector of Eqn (2.22) can be put in terms of displacement components via the geometric relations (Eqn (2.2)) as

$$\boldsymbol{\varepsilon} = \begin{bmatrix} \frac{\partial}{\partial x} & 0 & 0 \\ 0 & \frac{\partial}{\partial y} & 0 \\ 0 & 0 & \frac{\partial}{\partial z} \\ \frac{\partial}{\partial y} & \frac{\partial}{\partial x} & 0 \\ 0 & \frac{\partial}{\partial z} & \frac{\partial}{\partial y} \\ \frac{\partial}{\partial z} & 0 & \frac{\partial}{\partial x} \end{bmatrix} \cdot \begin{bmatrix} u \\ v \\ w \end{bmatrix} \quad (2.23)$$

Or, in terms of nodal displacement \mathbf{D} ,

$$\boldsymbol{\varepsilon} = \mathbf{A}\mathbf{D} \quad (2.24)$$

where

$$\mathbf{A} = \begin{bmatrix} \frac{\partial N_1}{\partial x} & 0 & 0 & \frac{\partial N_2}{\partial x} & 0 & 0 & \dots \\ 0 & \frac{\partial N_1}{\partial y} & 0 & 0 & \frac{\partial N_2}{\partial y} & 0 & \dots \\ 0 & 0 & \frac{\partial N_1}{\partial z} & 0 & 0 & \frac{\partial N_2}{\partial z} & \dots \\ \frac{\partial N_1}{\partial y} & \frac{\partial N_1}{\partial x} & 0 & \frac{\partial N_2}{\partial y} & \frac{\partial N_2}{\partial x} & 0 & \dots \\ 0 & \frac{\partial N_1}{\partial z} & \frac{\partial N_1}{\partial y} & 0 & \frac{\partial N_2}{\partial z} & \frac{\partial N_2}{\partial y} & \dots \\ \frac{\partial N_1}{\partial z} & 0 & \frac{\partial N_1}{\partial x} & \frac{\partial N_2}{\partial z} & 0 & \frac{\partial N_2}{\partial x} & \dots \end{bmatrix} \quad (2.25)$$

The entries in \mathbf{A} for the brick in Figure (2.1) (for example, in the x -direction) are defined as

$$\frac{\partial N_k}{\partial x} = \frac{\partial N_k}{\partial \xi} \cdot \frac{\partial \xi}{\partial x} \quad ; \quad \xi = \frac{x}{(a/2)} = \frac{2x}{a} \quad (2.26)$$

The same is true for η and ζ with y and z , respectively. ‘ a ’ is the width of the element in the x -direction from Figure (2.1). Recall, the shape functions N_k can be differentiated with respect to the local ξ - η - ζ coordinate system with help from Eqn (2.7).

In the virtual work formula of Eqn (2.18), $\bar{\mathbf{u}}$ and $\bar{\boldsymbol{\varepsilon}}$ represent virtual variations in the material’s displacement and strain fields, respectively. They depend upon nodal displacement variations in the same manner as the displacement field \mathbf{u} and strain $\boldsymbol{\varepsilon}$ depend on the actual nodal displacements. In other words,

$$\bar{\mathbf{u}} = \mathbf{N}\boldsymbol{\delta} \quad (2.27)$$

$$\bar{\boldsymbol{\varepsilon}} = \mathbf{A}\boldsymbol{\delta} \quad (2.28)$$

where $\boldsymbol{\delta}$ is the column matrix of virtual variations in nodal displacement arranged in the same convention as the actual nodal displacements \mathbf{D} (Eqn (2.6)).

Substituting Eqn (2.27), Eqn (2.28), and Eqn (2.20) for $\bar{\mathbf{u}}$, $\bar{\boldsymbol{\varepsilon}}$, and $\boldsymbol{\tau}$, respectively, into the virtual work formula in Eqn (2.18) yields $\mathbf{F}_{total} = \mathbf{f}$, where the external nodal forces are

$$\mathbf{F}_{total} = \sum_{m=1}^M \int_{S_m} \mathbf{N}^T \mathbf{T} dA + \sum_{m=1}^M \int_{V_m} \mathbf{N}^T \mathbf{b} dV - \left(\sum_{m=1}^M \int_{V_m} \rho \mathbf{N}^T \mathbf{N} dV \right) \ddot{\mathbf{D}} \quad (2.29)$$

where the first, second, and third right-hand side terms are the external nodal forces from surface tractions \mathbf{T} , body forces \mathbf{b} , and inertial forces $\rho \ddot{\mathbf{D}}$, respectively. $\ddot{\mathbf{D}}$ is the global vector of nodal accelerations for the whole material body (elements $1 \dots M$).

The internal nodal forces as a result of $\boldsymbol{\tau}$ are

$$\mathbf{f} = \mathbf{K}\mathbf{D} \quad (2.30)$$

where \mathbf{D} now represents the global vector of nodal displacements for all elements $1 \dots M$, determined by

$$\mathbf{D}_{global} = \sum_{m=1}^M \mathbf{D}_{local}^m \quad (2.31)$$

\mathbf{K} is referred to as the *global stiffness matrix*, and is defined as

$$\mathbf{K} = \sum_{m=1}^M \int_{V_m} \mathbf{A}^T \mathbf{C} \mathbf{A} dV \quad (2.32)$$

2.5 Provisions for Nearly Incompressible Materials

Soft tissue is regarded as a nearly incompressible material. Unfortunately, the basic finite element equations $\mathbf{F}_{total} = \mathbf{f}$ as defined in the previous section are poorly conditioned for numerical solution when a material's Poisson's ratio ν approaches 0.5. The problem arises due to \mathbf{C} in the stiffness matrix, \mathbf{K} ; \mathbf{C} contains the 1st Lamé constant λ , which tends to infinity as ν approaches 0.5. Thus, any small numerical errors are amplified when multiplied by λ - terms in the \mathbf{C} matrix. These now larger numerical errors can precipitate through the program to give erroneous values for the stress tensor $\boldsymbol{\tau}$ and the nodal displacement vector \mathbf{D} . This section discusses a way to remedy this situation, by going to the root of the problem and re-expressing terms in the basic equations of linear elasticity. These alterations affect the principle of virtual work, and hence the finite element equations for incompressible materials.

2.5.1 Principle of Virtual Work – Revisited

One way to eliminate \mathbf{C} from the finite element equations is to revisit the basic equations of linear elasticity and break the strain field into its deviatoric (shape change) and dilatational (volume change) parts, as shown below.

$$\varepsilon_{ij} = e_{ij} + \frac{1}{3} \varepsilon_v \delta_{ij} \quad (2.33)$$

where e_{ij} is the deviatoric strain, ε_v is the volumetric strain ($\varepsilon_v = \varepsilon_{11} + \varepsilon_{22} + \varepsilon_{33}$), and δ is the Kronecker delta. Note that Eqn (2.33) is merely a provision needed for incompressible materials: The geometric equations of Eqn (2.2) still apply.

The new expression for strain may be substituted into the constitutive relations of Eqn (2.5) to yield

$$\tau_{ij} = s_{ij} - P \delta_{ij}, \quad (2.34)$$

where s_{ij} is the deviatoric stress,

$$s_{ij} = 2\mu e_{ij}, \quad (2.35)$$

and P is the pressure within the element,

$$P = -\kappa \varepsilon_v, \quad (2.36)$$

where κ is the bulk modulus given by

$$\kappa = \frac{2}{3} \mu + \lambda \quad (2.37)$$

This new representation for stress τ_{ij} can be incorporated into the balance of momentum equations (Eqn (2.1)) and then multiplied by an arbitrary function \bar{u}_i to begin deriving the theorem of virtual work. However, the constraint equation

$$\varepsilon_v + \frac{P}{\kappa} = 0, \quad (2.38)$$

which is just a form of Eqn (2.36), must also be added to the momentum equation with a Lagrange multiplier \bar{P} . Thus, the altered momentum equation becomes

$$\frac{\partial s_{ij}}{\partial x_j} \bar{u}_i - \frac{\partial P}{\partial x_i} \bar{u}_i + (b_i - \rho \ddot{u}_i) \bar{u}_i + \left(\varepsilon_v + \frac{P}{\kappa} \right) \bar{P} = 0 \quad (2.39)$$

If the same steps were taken as in Section 2.3 to derive the theorem of virtual work, one would find that

$$\int_V \left(s_{ij} \bar{e}_{ij} - P \bar{\varepsilon}_v - \left(\varepsilon_v + \frac{P}{\kappa} \right) \bar{P} \right) dV = \int_S T_i \bar{u}_i dA + \int_V (b_i - \rho \ddot{u}_i) \bar{u}_i dV \quad (2.40)$$

where \bar{e}_{ij} and $\bar{\varepsilon}_v$ are defined, respectively, as

$$\bar{e}_{ij} = \frac{1}{2} \left(\frac{\partial \bar{u}_i}{\partial x_j} + \frac{\partial \bar{u}_j}{\partial x_i} \right) - \frac{1}{3} \bar{\varepsilon}_v \delta_{ij} \quad (2.41)$$

$$\bar{\varepsilon}_v = \frac{\partial u_i}{\partial x_i} \quad (2.42)$$

Eqn (2.40) is the virtual work theorem for linearly elastic, incompressible materials if \bar{u}_i , \bar{e}_{ij} , $\bar{\varepsilon}_v$, and \bar{P} represent virtual variations in the displacement field, deviatoric strain, volumetric strain, and pressure, respectively, for the material body.

2.5.2 The Revised Finite Element Equations

As it applies to the assembly of finite elements, the virtual work formula of Eqn (2.40) becomes

$$\sum_{m=1}^M \int_{V_m} \left(\bar{\mathbf{e}}^T \mathbf{s} - \bar{\varepsilon}_v^T P - \bar{P}^T \left(\varepsilon_v + \frac{1}{\kappa} P \right) \right) dV = \sum_{m=1}^M \int_{S_m} \bar{\mathbf{u}}^T \mathbf{T} dA + \sum_{m=1}^M \int_{V_m} \bar{\mathbf{u}}^T (\mathbf{b} - \rho \ddot{\mathbf{u}}) dV \quad (2.43)$$

for all elements $1 \dots M$.

In the finite element framework, there are only two true unknowns “hidden” in the virtual work formula of Eqn (2.43): nodal displacements \mathbf{D} and nodal pressures \mathbf{P} . All other variables can be written in terms of these nodal vectors.

There can be separate displacement nodes and pressure nodes in each element, which do not coincide. Figure (2.2) below shows this distinction for the brick element pictured in Figure (2.1), with eight displacement nodes and one pressure node.

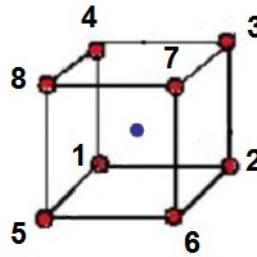


Figure 2.2

The eight node brick element used in the current investigation has one pressure node at its center, indicating that pressure is treated as a constant within each element of the model. Element pressure needs to be considered as part of the analysis for incompressible materials.

Analogous to the relationship between displacement field \mathbf{u} and nodal displacements \mathbf{D} , an element's pressure P depends upon nodal pressures \mathbf{P} via shape functions \mathbf{H} , shown below

$$P = \mathbf{H}\mathbf{P} \quad (2.44)$$

For an element with one pressure node, pictured in Figure (2.2), $\mathbf{H} = [1]$ for constant element pressure P . The virtual variation in pressure, \bar{P} , depends upon the variation in nodal pressure \mathbf{p} in the same manner that $\bar{\mathbf{u}}$ depends upon the variation in nodal displacement $\boldsymbol{\delta}$ as defined in Eqn (2.27):

$$\bar{P} = \mathbf{H}\mathbf{p} \quad (2.45)$$

If one defines

$$\mathbf{m}^T = [1 \quad 1 \quad 1 \quad 0 \quad 0 \quad 0], \quad (2.46)$$

volumetric strain ε_v can be written in terms of nodal displacement \mathbf{D} as

$$\varepsilon_v = \mathbf{A}_v \mathbf{D} \quad (2.47)$$

where the matrix \mathbf{A}_v is defined as

$$\mathbf{A}_v = \mathbf{m}^T \mathbf{A} \quad (2.48)$$

such that $\varepsilon_v = \varepsilon_{11} + \varepsilon_{22} + \varepsilon_{33}$, a 1x1 vector (scalar). In the virtual work formula (Eqn (2.43)),

the virtual variation of volumetric strain, $\bar{\varepsilon}_v$, depends upon $\bar{\boldsymbol{\delta}}$ rather than \mathbf{D} , as discussed for $\bar{\mathbf{u}}$ earlier.

If deviatoric stress \mathbf{s} and deviatoric strain \mathbf{e} are defined, respectively, as

$$\mathbf{s}^T = [s_{11} \quad s_{22} \quad s_{33} \quad s_{12} \quad s_{23} \quad s_{31}] \quad (2.49)$$

$$\mathbf{e}^T = [e_{11} \quad e_{22} \quad e_{33} \quad 2e_{12} \quad 2e_{23} \quad 2e_{31}] \quad (2.50)$$

Eqn (2.35) can be rewritten in matrix form as

$$\mathbf{s} = \mathbf{C}_d \mathbf{e} \quad (2.51)$$

where the matrix \mathbf{C}_d is defined as

$$\mathbf{C}_d = 2\mu \cdot \frac{1}{2} \begin{bmatrix} 2 & 0 & 0 & 0 & 0 & 0 \\ 0 & 2 & 0 & 0 & 0 & 0 \\ 0 & 0 & 2 & 0 & 0 & 0 \\ 0 & 0 & 0 & 1 & 0 & 0 \\ 0 & 0 & 0 & 0 & 1 & 0 \\ 0 & 0 & 0 & 0 & 0 & 1 \end{bmatrix} \quad (2.52)$$

\mathbf{s} can be written in terms of nodal displacement \mathbf{D} by first rewriting \mathbf{e} as

$$\mathbf{e} = \boldsymbol{\varepsilon} - \frac{1}{3} \mathbf{m} \varepsilon_v, \quad (2.53)$$

which is Eqn (2.33) rewritten in matrix form. Substituting Eqn (2.47) for ε_v , and using the definition of $\boldsymbol{\varepsilon}$ from Eqn (2.24), \mathbf{e} can be rewritten in terms of \mathbf{D} as

$$\mathbf{e} = \mathbf{A}_d \mathbf{D} \quad (2.54)$$

where the matrix \mathbf{A}_d is defined as

$$\mathbf{A}_d = \mathbf{I}_d \mathbf{A} \quad (2.55)$$

with \mathbf{I}_d defined as

$$\mathbf{I}_d = \mathbf{I} - \frac{1}{3} \mathbf{m} \mathbf{m}^T \quad (2.56)$$

Note, now, that $\bar{\mathbf{e}}$, the virtual variation of deviatoric strain in the element, depends upon the virtual variation in nodal displacement ($\boldsymbol{\delta}$) by

$$\bar{\mathbf{e}} = \mathbf{A}_d \boldsymbol{\delta} \quad (2.57)$$

With \mathbf{e} as defined in Eqn (2.54), \mathbf{s} can finally be written in terms of \mathbf{D} as

$$\mathbf{s} = \mathbf{C}_d \mathbf{A}_d \mathbf{D} \quad (2.58)$$

Finally, with all variables of the virtual work theorem (Eqn (2.43)) expressed in terms of either \mathbf{D} or \mathbf{P} , substitutions can be made similar to Section 2.4 to arrive at the finite element equations. But now, since there are two variables (\mathbf{D} and \mathbf{P}), terms containing the virtual displacements $\boldsymbol{\delta}$ and pressures \mathbf{p} can be grouped and written as a system of equations, shown below:

$$\begin{bmatrix} \mathbf{K}_{DD} & \mathbf{K}_{DP} \\ \mathbf{K}_{PD} & \mathbf{K}_{PP} \end{bmatrix} \cdot \begin{bmatrix} \mathbf{D} \\ \mathbf{P} \end{bmatrix} = \begin{bmatrix} \mathbf{F}_{total} \\ \mathbf{0} \end{bmatrix} \quad (2.59)$$

where \mathbf{D} and \mathbf{P} are the global vectors of nodal displacement and pressure, respectively, and \mathbf{F}_{total} is defined the same as in Eqn (2.29). The matrices \mathbf{K}_{DD} , \mathbf{K}_{DP} , \mathbf{K}_{PD} and \mathbf{K}_{PP} are defined, respectively, below

$$\mathbf{K}_{DD} = \sum_{m=1}^M \int_{V_m} \mathbf{A}_d^T \mathbf{C}_d \mathbf{A}_d dV \quad (2.60)$$

$$\mathbf{K}_{DP} = \sum_{m=1}^M \left(- \int_{V_m} \mathbf{A}_v^T \mathbf{H} dV \right) = \mathbf{K}_{PD}^T \quad (2.61)$$

$$\mathbf{K}_{PP} = \sum_{m=1}^M \left(- \int_{V_m} \frac{1}{\kappa} (\mathbf{H}^T \mathbf{H}) dV \right) \quad (2.62)$$

If element pressure P is constant, nodal pressure \mathbf{P} can be condensed out of the system given in Eqn (2.59) so that an effective “incompressible” stiffness matrix is formed, shown below:

$$\mathbf{K}_{inc} \mathbf{D} = \mathbf{F}_{total} \quad (2.63)$$

where \mathbf{K}_{inc} is defined as

$$\mathbf{K}_{inc} = \mathbf{K}_{DD} - \mathbf{K}_{DP} \mathbf{K}_{PP}^{-1} \mathbf{K}_{PD} \quad (2.64)$$

Formulating the finite element equations in this manner alleviates the difficulties associated with nearly incompressible materials. Although the bulk modulus, κ , in the numerator of \mathbf{K}_{PP}^{-1} in \mathbf{K}_{inc} goes to infinity as ν approaches 0.5, this apparently has no negative affect on global displacement \mathbf{D} .

Chapter 3

Static Analysis

3.1 Source Code

Free-access online source code designed in MATLAB (The MathWorks Inc., Natick, MA) by Zaicenco [16] was used as the basis from which to build a finite element model of soft tissue. This code was capable of building the global stiffness matrix derived in Section 2.4 for compressible material models. Additionally, it was capable of solving the system of equations

$$\mathbf{K}\mathbf{D} = \mathbf{F}, \quad (3.1)$$

where \mathbf{K} is the global stiffness matrix for compressible materials, \mathbf{D} is the global vector of nodal displacements, and \mathbf{F} is the first right-hand side term of \mathbf{F}_{total} in Eqn (2.29), which is repeated below for convenience.

$$\mathbf{F}_{total} = \sum_{m=1}^M \int_{S_m} \mathbf{N}^T \mathbf{T} dA + \sum_{m=1}^M \int_{V_m} \mathbf{N}^T \mathbf{b} dV - \left(\sum_{m=1}^M \int_{V_m} \rho \mathbf{N}^T \mathbf{N} dV \right) \ddot{\mathbf{D}}$$

If \mathbf{F} is a static force, solving for \mathbf{D} in Eqn (3.1) is called *static analysis*. Before addressing the dynamic problem with $\mathbf{F}(t)$, static analyses were first performed with the source code to assess the correctness of its original architecture and the subsequent alterations added for nearly incompressible materials.

3.1.1 Model Parameters

Since the original source code had been created by others, its accuracy was a matter of question. Therefore, it was necessary to first validate its results by some other means before moving

onward with the project. For this purpose, ANSYS (ANSYS Inc., Canonsburg, PA) was employed.

Table (3.1) below lists the parameters and specifications used to construct a *compressible* finite element model of soft tissue with the *original* source code.

Parameter	Value/ Specification
Dimensions	3 - x, y, z
Element type	8-node brick
Element size	4x4x4 mm
Shape functions, N_k	Linear, Eqn (2.7)
Model size	10x10x10 elements
Young's modulus, E	20 kPa
Poisson's ratio, ν	0.3
Boundary conditions	Surface $z = 0$, all DOF = 0

Table 3.1

Specifications used to construct a compressible finite element model with the original source code. The original source code could not handle the case of material incompressibility, so for an initial gauge of its accuracy, the code was tested as downloaded for a compressible model of soft tissue.

The element size (i.e., mesh size) was selected on the order of millimeters, which is comparable to the step size of the computer-controlled positioning system used by Maleke et al. [9,11,12] during HMI experiments (as explained previously in Section 1.3). A total model size of 40x40x40mm was chosen in accordance with a previous finite element simulation of USAE performed by Konofagou et al. [14]. This model size was also comparable to the size of excised tissue samples used by Konofagou and Hynynen [8] and Maleke et al. [11] in their experiments with HMI. 8-node brick elements were chosen to set up an easy node-numbering scheme, and linear shape functions were selected for simplicity. A Young's modulus (E) of 20kPa was selected to represent normal breast fat, which is in the appropriate range as observed by Krouskop et al. [5]. Poisson's ratio was set to 0.3 for a typical compressible material.

With the bottom surface ($z = 0$) fixed, u_x , u_y , and u_z for the first 11x11 nodes (due to the node-numbering scheme) were zero; this corresponded to the first 363 entries in the global displacement vector, \mathbf{D} . Since these displacements were already known (zero), these entries were removed from the displacement vector. Figure (3.1) provides an illustration of this procedure for the system of equations in Eqn (3.1).

$$\begin{array}{c}
 \text{363x363} \\
 \left[\begin{array}{cccccc} K_{1,1} & K_{1,2} & K_{1,3} & \cdots & \cdots & K_{1,3993} \\ K_{2,1} & K_{2,2} & K_{2,3} & \cdots & \cdots & K_{2,3993} \\ \vdots & \vdots & \vdots & \cdots & \cdots & \vdots \\ K_{363,1} & K_{363,2} & K_{363,3} & \ddots & \ddots & K_{363,3993} \\ \vdots & \vdots & \vdots & \ddots & \ddots & \vdots \\ K_{3993,1} & K_{3993,2} & K_{3993,3} & \cdots & \cdots & K_{3993,3993} \end{array} \right] \cdot \begin{bmatrix} u_x^1 = 0 \\ u_y^1 = 0 \\ \vdots \\ u_z^{121} = 0 \\ \vdots \\ u_z^{1331} \end{bmatrix} = \begin{bmatrix} F_x^1 \\ F_y^1 \\ \vdots \\ F_z^{121} \\ \vdots \\ F_z^{1331} \end{bmatrix} \\
 \text{3630x3630}
 \end{array}$$

Figure 3.1

An illustration of the reduction of the global stiffness matrix. Since the surface $z = 0$ of the model was fixed, the displacement at each node on that surface was known to be zero and could be removed from the displacement vector. The corresponding rows and columns of the stiffness matrix had to be removed as well because of linear algebra, thereby reducing the size of the problem.

The model had 1,331 nodes with three degrees of freedom (DOF) at each node. The global stiffness matrix \mathbf{K} and displacement vector \mathbf{D} had 3993x3993 and 3993x1 entries, respectively. However, since the first 363 entries of \mathbf{D} were zero from the fixed surface at $z = 0$, these entries were ignored (above the horizontal line in Figure (3.1)) and instead a “reduced” 3630x1 displacement vector was considered. The stiffness matrix was also reduced to comply with the rules of matrix multiplication; it consisted of the lower right-hand region of the global matrix circled in Figure (3.1). Thus, in the current investigation, static analysis actually consisted of determining the “reduced” displacement vector ($\mathbf{D}_{3630 \times 1}$) using the “reduced” stiffness matrix ($\mathbf{K}_{3630 \times 3630}$). So overall, the assumption of a fixed lower surface ($z = 0$) helped save computational time by reducing the size of the stiffness matrix.

A model with the above specifications was also constructed in ANSYS 10.0 using the SOLID45 element. In ANSYS, the SOLID45 element is used for the 3D modeling of structural solids. The element itself is defined by eight nodes having three DOF at each node: translations in the x , y , and z directions. Table (3.2) contains the ANSYS parameters used to construct the model described in Table (3.1).

Parameter	Value/ Specification
ELEMENT TYPE	BRICK 8 NODE 45 (SOLID 45)
MATERIAL MODEL	LINEAR, ELASTIC, ISOTROPIC
E	20000
NU	0.3
VOLUME DIMENSIONS X1, X2, Y1, Y2, Z1, Z2	0, 0.04, 0, 0.04, 0, 0.04
MESH TOOL - NDIV	10
MESH TOOL - SHAPE	HEX
STRUCTURAL DISPLACEMENT	ALL DOF = 0 on surface $z = 0$

Table 3.2

ANSYS specifications used to construct the compressible material model identified in Table 3.1.

3.1.2 Validating the Local Stiffness Matrix

An illustration of the general architecture of the original algorithm is depicted in Figure (3.2). The algorithm first computed the local stiffness matrix, which, for a homogeneous medium, was the same for each element. The construction of the local stiffness matrix thus provided a first step in assessing the accuracy of the source code. Rather than constructing a 10x10x10 element model, a 1x1x1 element model was made for this purpose instead. The same was done in ANSYS 10.0. For the source code algorithm, obtaining the local stiffness matrix was simple; it was a workspace variable in MATLAB. In ANSYS, however, the stiffness matrix was not obtainable; ANSYS does not consider the stiffness matrix a variable for viewing. Therefore, a strategy was devised to view the local stiffness matrix constructed by ANSYS.

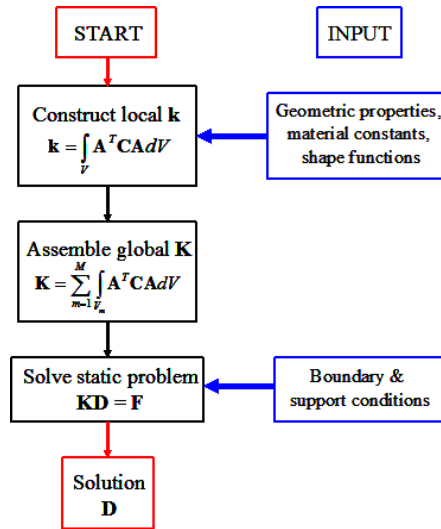


Figure 3.2

General architecture of the original source code. First the local stiffness matrix was constructed from material properties and shape functions, and was then assembled into the global stiffness matrix. The static problem could then be solved using the boundary and support conditions.

The single element MATLAB and ANSYS models are labeled with their nodes and coordinate systems in Figure (3.3) below. Notice that the coordinate system orientations and node-numbering schemes were different for each model.

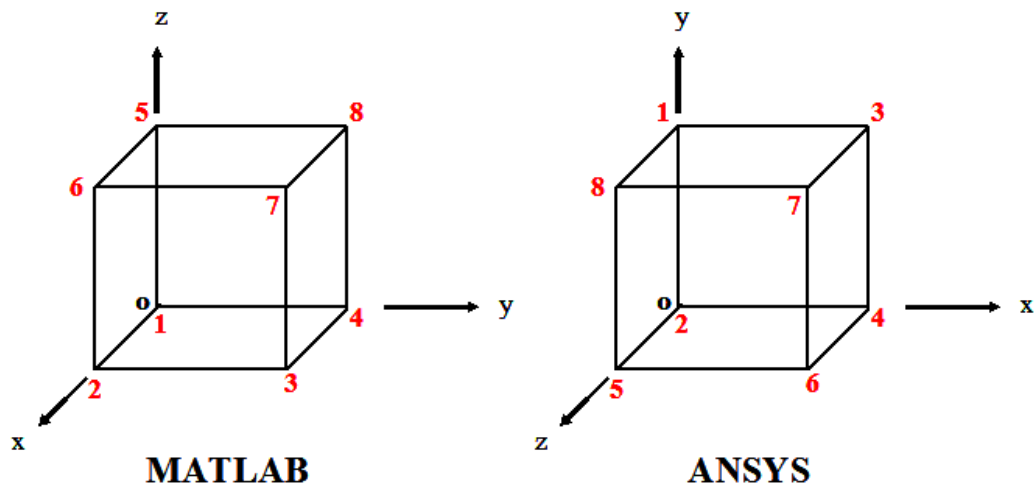


Figure 3.3

8-node brick elements used in MATLAB and ANSYS. Each element is labeled with a global coordinate system and node numbering scheme unique to the program it was constructed in.

To view the stiffness matrix in ANSYS, the scheme depicted in Figure (3.4) was employed using the governing equations $\mathbf{KD}=\mathbf{F}$ (Eqn (3.1)). Note the use of a unit displacement; for this analysis, the models were 100x100x100 units in keeping with the assumption of small deformations.

$$\begin{bmatrix} K_{1,1} & K_{1,2} & \cdots & K_{1,24} \\ K_{2,1} & K_{2,2} & \cdots & K_{2,24} \\ \vdots & \vdots & \ddots & \vdots \\ K_{24,1} & K_{24,2} & \cdots & K_{24,24} \end{bmatrix} \cdot \begin{bmatrix} u_x^1 = 1 \\ u_y^1 = 0 \\ \vdots \\ u_z^8 = 0 \end{bmatrix} = \begin{bmatrix} F_x^1 \\ F_y^1 \\ \vdots \\ F_z^8 \end{bmatrix}$$

Figure 3.4

An illustration of the scheme used to view the local stiffness matrix constructed in ANSYS. Since the stiffness matrix is not a variable for viewing in ANSYS, this scheme was devised using operations and variables possible in the program. This was needed to assess the validity of the local stiffness matrix constructed with the original source code.

Figure (3.4) indicates that if all entries in vector \mathbf{D} were zero except for one (and if that entry equals “1”), then by matrix multiplication, the force vector would equal the column in the stiffness matrix corresponding to the nonzero row entry of the displacement vector. This scheme was executed in ANSYS; a unit displacement was applied to a given node and the reaction forces (force vector) were viewed in the post-processor.

For example, if $u_x^2 = 1$ was set in ANSYS, the resulting reaction forces corresponded to the 2nd column of the local stiffness matrix computed by MATLAB. This was because the x-direction at node 2 in ANSYS equaled the y-direction at node 1 in MATLAB (see Figure (3.3)); in MATLAB, u_y^1 was the 2nd row entry of the displacement vector \mathbf{D} (see Figure (3.4)), which corresponded to the 2nd column of \mathbf{K} . Figure (3.5) shows some additional displacement equivalencies between MATLAB (left) and ANSYS (right), which can be inferred from Figure (3.3).

$$\begin{bmatrix} u_x^1 \\ u_y^1 \\ u_z^1 \\ u_x^2 \\ \vdots \\ u_z^8 \end{bmatrix} = \begin{bmatrix} u_z^2 \\ u_x^2 \\ u_y^2 \\ u_z^5 \\ \vdots \\ u_y^3 \end{bmatrix}$$

Figure 3.5

Displacement equivalencies between MATLAB (left) and ANSYS (right). Since the orientation of the global coordinate systems and the node numbering schemes for each element are different in MATLAB and ANSYS, the displacement at one node in one direction in MATLAB is equivalent to the displacement at a node with another number in another direction in ANSYS.

The first eight entries of the 2nd column of the local stiffness matrix computed by MATLAB alongside the reaction forces from setting $u_x^2 = 1$ and all other DOF = 0 in ANSYS are depicted in Figure (3.6). In the MATLAB node-numbering scheme, the corresponding row entries of the displacement and force vectors are denoted next to the stiffness column (see Figure (3.4)). Comparing the ANSYS reaction forces to the MATLAB stiffness entries was facilitated by the displacement equivalencies in Figure (3.5). These equivalencies also applied between the force entries in MATLAB and the reaction forces from ANSYS. Since the forces computed by ANSYS were reaction forces, they were opposite in sign to the entries in the stiffness matrix.

From Figure (3.6), it could be seen that the source code and ANSYS were in accordance for the 2nd column of \mathbf{K} . By repeating this process for other nodes in ANSYS, it was confirmed that the source code was capable of accurately generating the local stiffness matrix for a compressible material model.

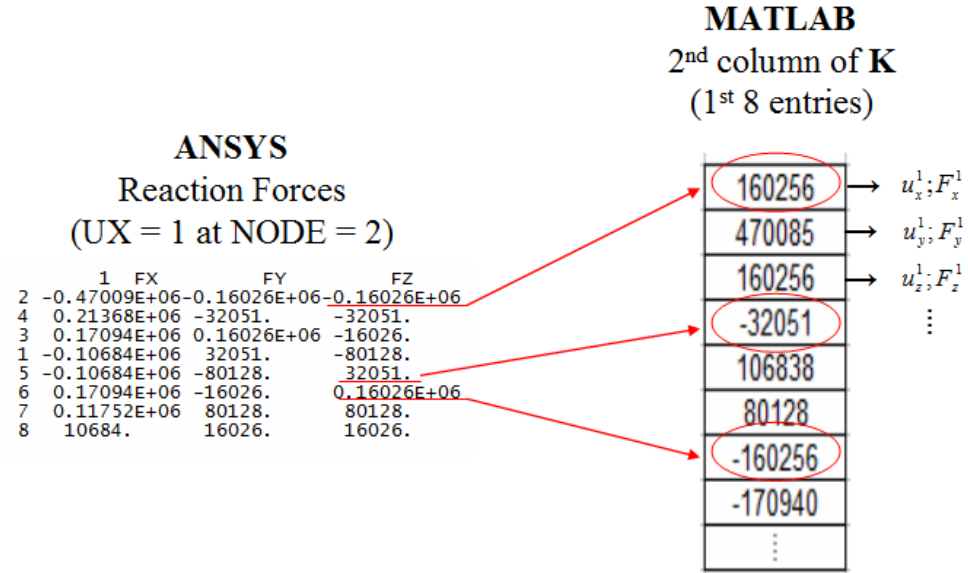


Figure 3.6

The reaction forces of ANSYS versus the corresponding column of the local compressible stiffness matrix from the MATLAB source code. Each row of the stiffness “column” is denoted by the corresponding row entry of the displacement and force vectors. The displacement equivalencies discussed in Figure (3.5) apply to forces as well and aid in the comparison.

3.1.3. Validating the Global Stiffness Matrix

Although the local stiffness matrix had been validated by ANSYS, the assembly routine used by the source code to create the global stiffness matrix was still up to question. The only way to assess this routine was to perform static analyses with both the source code and ANSYS and then compare the displacement solution. The models in both MATLAB and ANSYS were constructed according to the specifications shown in Table (3.1) and Table (3.2), respectively.

A constant force was applied to the geometrically central node in each model. For a 40x40x40mm model, the force was placed at coordinate (20,20,20)mm. The magnitude of this force was 0.01N, and it was applied in the z -direction towards the fixed surface. Thus, the force vector \mathbf{F} was zero everywhere except for F_z at the node with coordinates (20,20,20)mm.

Figure (3.7) illustrates the 10x10x10 element models used in MATLAB and ANSYS loaded at point (20,20,20)mm. Note the orientation of the coordinate systems and force.

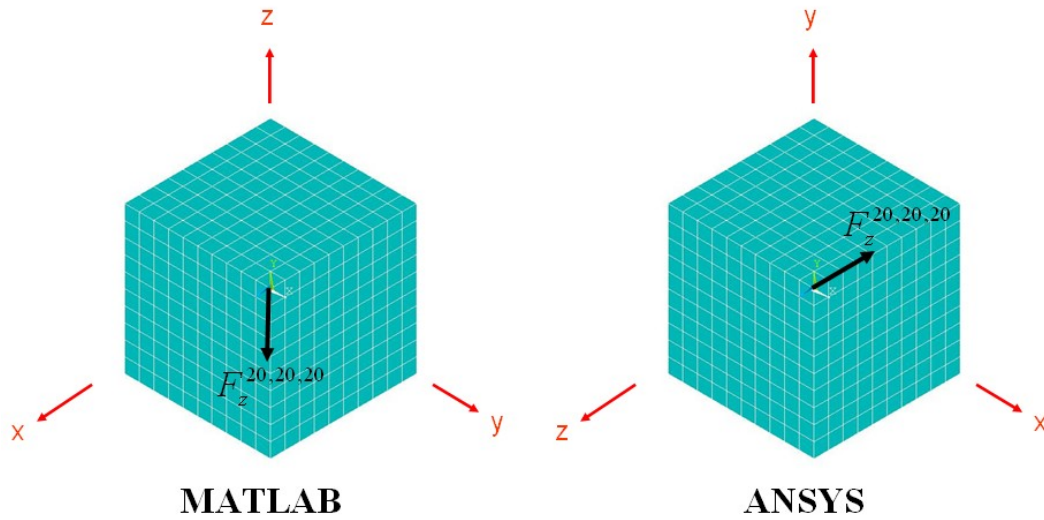


Figure 3.7

10x10x10 element models used in MATLAB and ANSYS. Each model is labeled with its global coordinate system unique to the program it was constructed in. A force was applied at the geometrically central node which, for a 4mm mesh, translates to coordinate (20,20,20)mm. The force was applied towards the fixed surface at $z = 0$ (in the negative z -direction).

The source code solved Eqn (3.1) by

$$\mathbf{D} = \mathbf{K}^{-1}\mathbf{F} \quad (3.2)$$

where \mathbf{K}^{-1} was computed using the `inv(.)` command in MATLAB.

The source code determined \mathbf{D} as a single column vector arranged in the standard form shown in Eqn (2.6), stated again below for convenience.

$$\mathbf{D} = \begin{bmatrix} U_1 \\ V_1 \\ W_1 \\ U_2 \\ \vdots \\ W_N \end{bmatrix}$$

Recall that U , V , and W indicate the x , y , and z displacements, respectively, at nodes $1 - N$. In contrast, ANSYS did not incorporate the x , y , and z displacements into a single displacement vector, but instead used separate vectors for each direction, shown below.

$$UX = \begin{bmatrix} U_1 \\ U_2 \\ \vdots \\ U_N \end{bmatrix}, UY = \begin{bmatrix} V_1 \\ V_2 \\ \vdots \\ V_N \end{bmatrix}, UZ = \begin{bmatrix} W_1 \\ W_2 \\ \vdots \\ W_N \end{bmatrix} \quad (3.3)$$

The difficulty in comparing \mathbf{D} from MATLAB and ANSYS arose from the fact that the nodes were not labeled using the same node-numbering convention (as seen in Figure (3.3)). Thus, coordinates, not node numbers, were used as the index with which to compare the displacement results.

By comparing the x , y , and z displacement at each nodal coordinate, a maximum percent error of 0.0042% was found between MATLAB and ANSYS results. This finding confirmed the correctness of the routine used by the source code to assemble the global stiffness matrix for a compressible material. It also affirmed that the support and loading conditions were applied correctly in each program.

3.2 Source Code Alterations

The original source code's formulation of the local (compressible) stiffness matrix \mathbf{K} was altered for material incompressibility, as discussed in Section 2.5. Once these programming changes were implemented into the source code, ANSYS 10.0 had to be used once again in order to confirm the correctness of the alterations.

3.2.1 Model Parameters

With the altered source code, a 1x1x1 element model 100x100x100 units in size was used to generate the local incompressible stiffness matrix. This model was identical to that described in Table (3.1), except Poisson's ratio now equaled 0.495 to mimic a nearly incompressible material. Table (3.3) shows the ANSYS parameters needed to construct this incompressible model.

Parameter	Value/ Specification
ELEMENT TYPE	BRICK 8 NODE 185 (SOLID 185)
ELEMENT FORMULATION	MIXED U/P
INTEGRATION METHOD	FULL
MATERIAL MODEL	LINEAR, ELASTIC, ISOTROPIC
E	20000
NU	0.495
VOLUME DIMENSIONS X1, X2, Y1, Y2, Z1, Z2	0, 100, 0, 100, 0, 100
MESH TOOL - NDIV	1
MESH TOOL - SHAPE	HEX

Table 3.3

ANSYS specifications used to construct an incompressible material element. A model of this type in ANSYS was needed to assess the accuracy of the programming modifications added to the original source code to handle the case of material incompressibility.

The SOLID185 element ('ELEMENT TYPE' in Table (3.3)) had the same basic properties as the SOLID45 element, but it also had the capability of simulating the deformation of nearly incompressible materials with the 'MIXED U/P' element option. The term 'mixed u/p' is used to describe the formulation of the stiffness matrix described in Section 2.5 for nearly incompressible materials, where displacement 'u' and pressure 'p' were treated as independent variables inside each element.

3.2.2 Validating the Altered Local Stiffness Matrix

To compare the local incompressible stiffness matrices from both the altered source code and ANSYS, the same procedure was followed as in Section 3.1.2 for the compressible case. All displacement equivalencies (see Figure 3.5)) between the MATLAB and ANSYS models still applied, as did the reasoning from that Section.

The first eight entries of the 2nd column of the local *incompressible* stiffness matrix computed by the altered source code alongside the reaction forces resulting from setting $u_x^2 = 1$ and all other DOF = 0 in ANSYS are depicted in Figure (3.8). In the MATLAB node-numbering scheme, the corresponding row entries of the displacement and force vectors are denoted next to the stiffness column (see Figure (3.4)). Comparing the ANSYS reaction forces to the MATLAB stiffness entries was facilitated by the displacement equivalencies in Figure (3.5). These equivalencies also applied between the force entries in MATLAB and the reaction forces from ANSYS. Since the forces computed by ANSYS were reaction forces, they were opposite in sign to the entries in the stiffness matrix.

From Figure (3.8), it was apparent that the source code (altered) and ANSYS were in accordance for the 2nd column of \mathbf{K}_{inc} . By repeating this process for other nodes in ANSYS, it was confirmed that the altered source code was capable of accurately generating the local stiffness matrix for a nearly incompressible material model; the provisions according to Section 2.5 were implemented correctly.

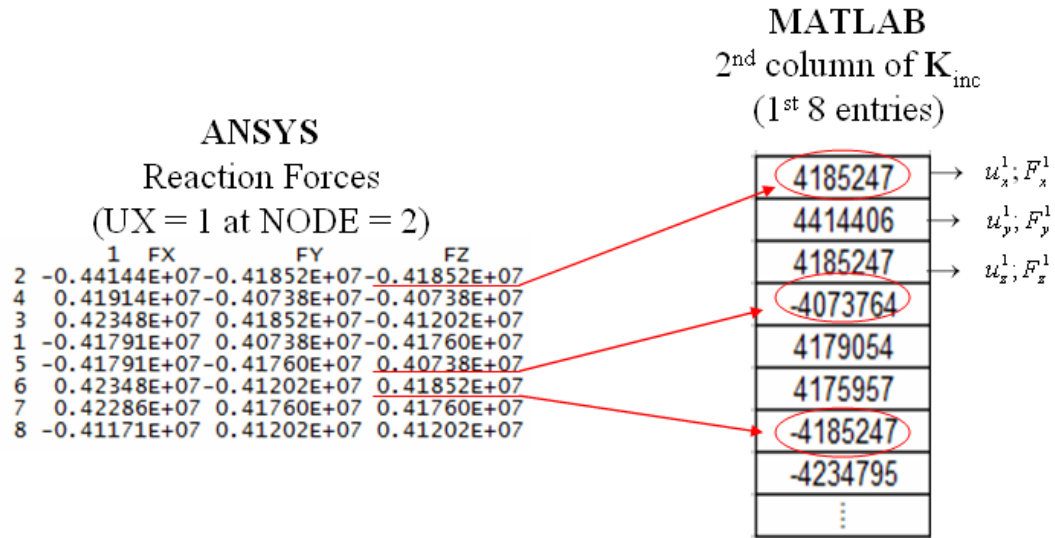


Figure 3.8

The reaction forces of ANSYS versus the corresponding column of the local incompressible stiffness matrix from the MATLAB source code. Each row of the stiffness “column” is denoted by the corresponding row entry of the displacement and force vectors. The displacement equivalencies discussed in Figure (3.5) apply to forces as well and aid in the comparison.

Chapter 4

Dynamic Analysis

4.1 Finite Element Equations of Motion

Recall from Section 1.3 that harmonic motion imaging is a dynamic excitation method. Thus, to simulate results obtained with this technique, the excitation or force applied to the current soft tissue model had to be dynamic as well. In finite element modeling, for a multiple degree of freedom system, this requires a time-varying nodal force vector, $\mathbf{F}(t)$.

In structural mechanics, the system of equations

$$\mathbf{M}\ddot{\mathbf{D}}(t) + \mathbf{V}\dot{\mathbf{D}}(t) + \mathbf{K}\mathbf{D}(t) = \mathbf{F}(t) \quad (4.1)$$

are considered the general finite element equations of motion for a material under dynamic excitation. \mathbf{M} , \mathbf{V} , and \mathbf{K} are the global mass, damping, and stiffness matrices, respectively. $\mathbf{F}(t)$ is the global vector of time-varying, externally applied nodal forces, and $\mathbf{D}(t)$, $\dot{\mathbf{D}}(t)$, and $\ddot{\mathbf{D}}(t)$ represent the time-varying global vectors of nodal displacements, velocities, and accelerations, respectively, induced in the medium by $\mathbf{F}(t)$.

Even though Fung [17], the “father of modern biomechanics”, noted that biological tissues have viscoelastic features, the current soft tissue model was viewed as an elastic material ($\mathbf{V} = \mathbf{0}$). Viscosity effects will be addressed in future work, and were not considered in depth in the current investigation. Thus, the general finite element equations above reduce to

$$\mathbf{M}\ddot{\mathbf{D}}(t) + \mathbf{K}\mathbf{D}(t) = \mathbf{F}(t), \quad (4.2)$$

which are the finite element equations of motion for an elastic material. In the current investigation, $\mathbf{K} = \mathbf{K}_{inc}$ to model nearly incompressible soft tissue.

4.1.1 Mass Matrix

The mass matrix \mathbf{M} originates from the last right-hand side term of \mathbf{F}_{total} in Eqn (2.29), stated again below for convenience.

$$\mathbf{F}_{total} = \sum_{m=1}^M \int_{S_m} \mathbf{N}^T \mathbf{T} dA + \sum_{m=1}^M \int_{V_m} \mathbf{N}^T \mathbf{b} dV - \left(\sum_{m=1}^M \int_{V_m} \rho \mathbf{N}^T \mathbf{N} dV \right) \ddot{\mathbf{D}}$$

Unlike static analysis, the vector of external nodal forces \mathbf{F}_{total} is a function of time in the dynamic problem, as is the resulting displacement $\mathbf{D}(t)$. Thus, the second time derivative of displacement ($\ddot{\mathbf{D}}$) is nonzero, and the last right-hand side term of \mathbf{F}_{total} enters into the finite element equations. If body forces \mathbf{b} are neglected, the balance of internal to external nodal forces given by

$$\mathbf{K}\mathbf{D} = \mathbf{F}_{total} \quad (4.3)$$

(as discussed in Section 2.4) forms the finite element equations of motion (Eqn (4.2))

$$\mathbf{M}\ddot{\mathbf{D}}(t) + \mathbf{K}\mathbf{D}(t) = \mathbf{F}(t),$$

where \mathbf{M} is defined from \mathbf{F}_{total} as

$$\mathbf{M} = \sum_{m=1}^M \int_{V_m} \rho \mathbf{N}^T \mathbf{N} dV \quad (4.4)$$

As mentioned in Section 4.1, $\mathbf{F}(t)$ in Eqn (4.2) is the global vector of time-varying, externally applied nodal forces; it is the first right-hand side term of $\mathbf{F}_{total}(t)$.

Rather than using shape functions \mathbf{N} to determine the mass matrix, a direct approach can be used by concentrating the total mass of the material body at its nodes. This technique is called “lumping”, and is illustrated in Figure (4.1) for a two-dimensional body with rectangular elements.

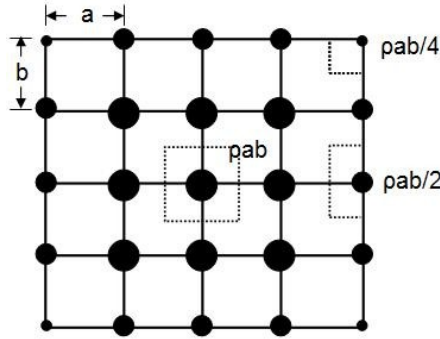


Figure 4.1

The lumped mass approach used to formulate the mass matrix in the current simulation, where the mass of each element is assumed to reside at its nodes. ‘a’ and ‘b’ denote the edge lengths of each element, and ρ is the material density. Depending upon location, the mass at each node will vary accordingly, and is some factor of $m = \rho ab$.

In Figure (4.1), the total mass of the material surrounding each node (illustrated by dashed lines) is treated as a point mass at that node (denoted by a black circle). The size of each circle corresponds to how much mass is concentrated at a given node, which is related to its position in the model (interior, edge, or corner). If the density of the material is ρ and each rectangular element has dimensions ‘a’ x ‘b’, the mass at interior nodes, for example, is $m = \rho ab$. The same reasoning can be applied to edge nodes and corner nodes.

The lumped mass approach has been found to work well in practice as long as all mass is accounted for. Reportedly, there is no discernible increase in solution accuracy when the generalized mass formulation (Eqn (4.4)) is used. Thus, for simplicity, the mass matrix \mathbf{M} in this investigation was formed using the lumped mass approach.

4.1.2 Force Vector

Any force applied to the current soft tissue model should be consistent with what is used and observed by other researchers working with acoustic radiation force. Equation (4.5) below is an approximation to the acoustic radiation force; appropriately, it was used to define the forcing function applied to the current soft tissue model.

$$F_o(t) = \frac{2\alpha(f)I(t)}{c} \cdot V \quad (4.5)$$

f , $I(t)$, and V are the operating frequency, time-varying intensity, and focal volume, respectively, of the acoustic radiation force-generating FUS transducer(s) [8]. The speed of sound in the tissue is c . The frequency-dependent absorption coefficient of the tissue is $\alpha(f)$. In this investigation, the attenuation of the material was assumed to be linear with frequency so that absorption $\alpha(f) = \alpha:f$. This assumption was used by Palmeri et al. [18] in their method to characterize a material's attenuation using acoustic radiation force.

Figure (4.2) provides a schematic of the HMI experimental setup used by Maleke et al. [12]. The variables described in Eqn (4.5), as well as another pertinent variable ('*freq*'), are illustrated in relation to the setup. The variable *freq* will be explained shortly.

The temporal characteristics of $F_o(t)$ depend directly upon intensity $I(t)$. Konofagou and Hynynen [8], for example, likened $I(t)$ to a nonnegative harmonic wave in their simulation of HMI. This assumption for the form of $I(t)$ was used as the basis from which to define the forcing function for the current soft tissue model.

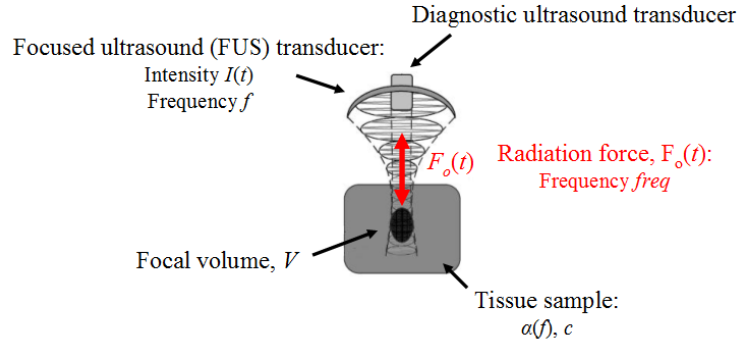


Figure 4.2

A schematic of harmonic motion imaging. A focused ultrasound (FUS) transducer of intensity $I(t)$ operating at a frequency f excites a small volume of tissue (V), with an acoustic absorption coefficient α dependent upon frequency f . Sound travels in the tissue at speed c . An acoustic radiation force $F_o(t)$ is generated in the tissue, which oscillates at frequency $freq$. A diagnostic ultrasound transducer monitors the resulting tissue oscillations.

The forcing function $F_o(t)$ used in this investigation is defined below as

$$F_o(t) = f_o + f_o \sin\left(\omega t - \frac{\pi}{2}\right) \quad (4.6)$$

The angular frequency ω in Eqn (4.6) is given by

$$\omega = 2\pi \cdot freq, \quad (4.7)$$

where $freq$ is defined as the oscillating frequency of the acoustic radiation force, shown in Figure (4.2). f_o is defined as the temporal average of $F_o(t)$ from Eqn (4.5).

Point-like acoustic radiation force, such as that used during HMI experimentation, can be likened to a nodal force in finite element modeling. In HMI, only one direction at one point can be loaded in any one transducer configuration. Thus, in the current investigation, the nodal force vector was defined accordingly and is described next.

The global force vector in the equations of motion (Eqn (4.2)) was defined as

$$\mathbf{F}(t) = \begin{bmatrix} 0 \\ \vdots \\ 0 \\ -F_o(t) \\ 0 \\ \vdots \\ 0 \end{bmatrix} . \quad (4.8)$$

This notation is meant to indicate that in any one configuration, $F_o(t)$ was applied to a single node in a single direction only; the force vector was zero everywhere else. In the current investigation, the z -direction was chosen as the direction of loading. The forcing function $F_o(t)$ was always applied towards the fixed surface of the model at $z = 0$ (hence, the negative sign on $F_o(t)$).

To load different nodes within the model to mimic a computer-controlled positioning system, separate force vectors must be defined for each case. This also implies that each loading point requires its own configuration of the equations of motion. Figure (4.3) illustrates this concept for several scanned points.

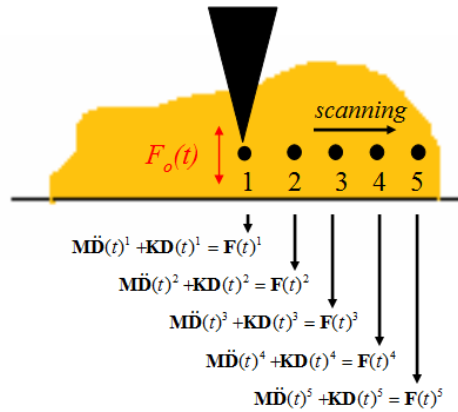


Figure 4.3

Multiple equilibrium configurations of HMI. During experimentation, the acoustic radiation force (i.e., the forcing function $F_o(t)$ in FEM) can only be applied to one point at a time. In the current finite element simulation, this necessitates a unique force vector $\mathbf{F}(t)$ and a unique set of equilibrium equations for each point scanned.

4.1.3 Model Parameters for Dynamic Analysis

The parameters used to define the material matrices \mathbf{M} and \mathbf{K}_{inc} and the force vector $\mathbf{F}(t)$ in the dynamic analysis of the current soft tissue model are listed in Table (4.1). All geometric properties from Table (3.1) still apply except where re-defined in Table (4.1).

Symbol	Description	Found in:	Value(s)	Units
ρ	Density	\mathbf{M}	1100	kg/m ³
E	Young's modulus	\mathbf{K}_{inc}	20 - 60	kPa
ν	Poisson's ratio	\mathbf{K}_{inc}	0.495	-
$\alpha(f)$	Absorption coeff.	$\mathbf{F}(t)$	1	dB/cm/MHz
f	Transducer frequency	$\mathbf{F}(t)$	4	MHz
i_o	Temporal average of intensity, $I(t)$	$\mathbf{F}(t)$	500	W/cm ²
c	Speed of sound in tissue	$\mathbf{F}(t)$	1540	cm/s
V	Focal volume	$\mathbf{F}(t)$	0.004	cm ³
$freq$	Acoustic radiation force frequency	$\mathbf{F}(t)$	50 - 400	Hz

Table 4.1

Model parameters used in the current dynamic simulation of soft tissue. The material constants used to define the mass and incompressible stiffness matrices are shown, as well as the parameters used to define the forcing function $F_o(t)$.

The density (ρ) of the model was picked as the density of the tissue-mimicking gelatin gels used by Maleke et al. [12] for their HMI experimentation. The values of Young's modulus (E) fall within the range observed by Krouskop et al. [5] for normal fat and glandular breast tissue. This range of Young's modulus has also been used by Konofagou and Hynynen [8] in their finite element simulations of HMI, and also by Maleke et al. [12] in their experiments on calibrated tissue-mimicking phantoms. Since soft tissue is considered a nearly incompressible material with Poisson's ratio (ν) approaching 0.5, a value of 0.495 was chosen in accordance with that used by Krouskop et al. [5].

The absorption coefficient ($\alpha(f)$) used in the current investigation was defined from the attenuations of homogeneous, tissue-mimicking phantoms used by Palmeri et al. [18]. It was assumed that all attenuation is due to absorption, thus defining the absorption coefficient used here. Transducer frequency (f) was taken between the operating frequencies used by Konofagou and Hynynen [8] and Maleke et al. [12] in their experimentation with HMI. For subsequent data comparison, the acoustic radiation force frequency ($freq$) was also chosen in accordance with references [8] and [12]. Nightingale et al. [19] used a temporal average intensity (i_o) of several W/cm^2 for inducing displacement in calibrated tissue phantoms, while Maleke et al. [12] used nearly $1000 W/cm^2$ for ablating bovine liver. In the current investigation, i_o was taken as the median of these two extremes to define an acoustic intensity capable of displacing tissue without ablating it. To define the amplitude of the nodal force as it was applied to the current soft tissue model (f_o in Eqn (4.6)), i_o was used as opposed to $I(t)$ in Eqn (4.5) to compute the value $f_o = 0.01N$.

The speed of sound in tissue (c) was taken as $1540m/s$, which was indicated by Palmeri et al. [18]. Lastly, the focal volume (V) of the acoustic force-generating FUS transducer was taken within $1 - 8 mm^3$, which, according to Nightingale et al. [13], is the typical range for the volume of tissue to which point-like radiation force is applied.

4.2 Newmark Method

The Newmark method was used to solve the dynamic problem for the current soft tissue model. It is a popular technique used by engineers to determine the dynamic response of a structure under the action of any general time-dependent load. It was chosen in this investigation mainly because it is very generalized; no assumptions restrict the form of allowable forcing functions. This may be beneficial in future analyses involving forcing functions more complicated than the simple harmonic wave used here.

The fundamental approximations of the Newmark method were used to help solve the dynamic problem for $\mathbf{D}(t)$, and are shown in Eqn (4.9) and Eqn (4.10) below.

$$\dot{\mathbf{D}}_i = \alpha h \ddot{\mathbf{D}}_i + \dot{\mathbf{D}}_{i-1} + (1 - \alpha) h \ddot{\mathbf{D}}_{i-1} \quad (4.9)$$

$$\mathbf{D}_i = \beta h^2 \ddot{\mathbf{D}}_i + \mathbf{D}_{i-1} + h \dot{\mathbf{D}}_{i-1} + \left(\frac{1}{2} - \beta \right) h^2 \ddot{\mathbf{D}}_{i-1} \quad (4.10)$$

In Eqn (4.9) and Eqn (4.10), \mathbf{D}_i , $\dot{\mathbf{D}}_i$, and $\ddot{\mathbf{D}}_i$ represent *unknown* vectors of nodal displacement, velocity, and acceleration, respectively, at some finite time t . \mathbf{D}_{i-1} , $\dot{\mathbf{D}}_{i-1}$, and $\ddot{\mathbf{D}}_{i-1}$ represent *known* vectors of nodal displacement, velocity, and acceleration, respectively, determined one time step h earlier. α and β are arbitrary constants known as *Newmark parameters*; these parameters will be discussed in more detail in the next section.

The fundamental approximations of Eqn (4.9) and Eqn (4.10) were used to iteratively solve for $\mathbf{D}(t)$ in Eqn (4.1) in finite time intervals. (Note: In dynamic analysis with the Newmark method, Eqn (4.1) was used for the current model with \mathbf{V} set equal to $\mathbf{0}$ because damping was not considered in the current investigation.)

Using index notation, the general finite element equations in Eqn (4.1) become

$$\mathbf{M} \ddot{\mathbf{D}}_i + \mathbf{V} \dot{\mathbf{D}}_i + \mathbf{K}_{inc} \mathbf{D}_i = \mathbf{F}_i, \quad (4.11)$$

where $\mathbf{K} = \mathbf{K}_{inc}$ for material incompressibility. In order to solve for the displacement vector at each iteration in time, the fundamental approximations are used to eliminate $\dot{\mathbf{D}}_i$ and $\ddot{\mathbf{D}}_i$ from Eqn (4.11) such that \mathbf{D}_i is the only unknown.

From Eqn (4.10),

$$\ddot{\mathbf{D}}_i = \frac{1}{\beta h^2} \mathbf{D}_i - \mathbf{F}_a \quad (4.12)$$

where \mathbf{F}_a is a known vector defined as

$$\mathbf{F}_a = \frac{1}{\beta h^2} \left(\mathbf{D}_{i-1} + h\dot{\mathbf{D}}_{i-1} + \left(\frac{1}{2} - \beta \right) h^2 \ddot{\mathbf{D}}_{i-1} \right). \quad (4.13)$$

Plugging Eqn (4.12) into Eqn (4.9) for $\ddot{\mathbf{D}}_i$ yields a new value for $\dot{\mathbf{D}}_i$:

$$\dot{\mathbf{D}}_i = \frac{\alpha}{\beta h} \mathbf{D}_i - \mathbf{F}_b, \quad (4.14)$$

where \mathbf{F}_b is a known vector defined as

$$\mathbf{F}_b = \alpha h \mathbf{F}_a - \dot{\mathbf{D}}_{i-1} - (1 - \alpha) h \ddot{\mathbf{D}}_{i-1}. \quad (4.15)$$

Thus, in light of Eqn (4.12) and Eqn (4.14), the equations of motion in Eqn (4.11) reduce to the equivalent “static” form

$$\overline{\mathbf{K}} \mathbf{D}_i = \overline{\mathbf{F}}_i \quad (4.16)$$

where \mathbf{D}_i is the solution to the dynamic problem at a finite time t . $\overline{\mathbf{K}}$ and $\overline{\mathbf{F}}_i$ are the modified stiffness matrix and effective force vector, respectively, defined as

$$\overline{\mathbf{K}} = \frac{1}{\beta h^2} \mathbf{M} + \frac{\alpha}{\beta h} \mathbf{V} + \mathbf{K}_{inc} \quad (4.17)$$

$$\overline{\mathbf{F}}_i = \mathbf{F}_i + \mathbf{M} \mathbf{F}_a + \mathbf{V} \mathbf{F}_b \quad (4.18)$$

Recall that in the current investigation, $\mathbf{V} = \mathbf{0}$ (Eqns (4.17) and (4.18) encompass a general material). If α and β are nonzero, \mathbf{D}_i at each point in time depends upon the vector of applied force at that same time (\mathbf{F}_i) and on the immediately previous time solutions of \mathbf{D}_{i-1} , $\dot{\mathbf{D}}_{i-1}$, and $\ddot{\mathbf{D}}_{i-1}$ (see Eqns (4.18), (4.13), and (4.15) for $\overline{\mathbf{F}}_i$, \mathbf{F}_a , and \mathbf{F}_b , respectively). For example, if

starting from $i = 1$ (time $t = h$), $\mathbf{D}_1 = \mathbf{D}_1(\mathbf{D}_0, \dot{\mathbf{D}}_0, \ddot{\mathbf{D}}_0, \mathbf{F}_1)$. By iteratively repeating an $i = i + 1$ process, the whole $\mathbf{D}(t)$ can be determined in i time steps h .

4.2.1 Newmark Method Parameters

The parameters used during the dynamic analysis of the current soft tissue model with the Newmark method are shown in Table (4.2).

Symbol	Description	Value/Expression	Units
α	Newmark parameter	1/2	-
β	Newmark parameter	1/4	-
h	Time step	T/N	s
T	Period of loading force	$1/freq$	s
N	Samples per loading period	30	-
t	Total time for analysis	$PER * T$	s
PER	Number of loading periods	75	-

Table 4.2

Parameters used during the current dynamic finite element analysis of a soft tissue model with the Newmark method. Time step h and the time for analysis t cannot be arbitrarily assigned; convergence analyses were performed for N and PER to assess the optimal values of these parameters, respectively.

α , β , and h are the Newmark parameters and time step, respectively, from the previous section. In this investigation, h was defined as T/N , where T was the period of the forcing function $F_o(t)$ (with frequency $freq$ as discussed in Section 4.1.2), and N was the number of samples per loading period. t was the total time for the analysis in which $\mathbf{D}(t)$ was to be determined. t was defined by $PER * T$, where PER was the number of loading periods applied.

In the current investigation, the parameters α , β , N , and PER in Table (4.2) determined the efficacy of the Newmark method in solving the finite element equations of motion. As stated by Dill [20], the fundamental issues considered were those of solution stability, convergence, and error.

The general Newmark method is unconditionally stable for the values of α and β below [20].

$$\alpha \geq \frac{1}{2} \quad (4.19)$$

$$\beta = \frac{(\alpha + 1/2)^2}{4} \quad (4.20)$$

When neither α nor $\beta = 0$, the Newmark method is said to be *implicit*, meaning that $\mathbf{D}(t)$ at time $t = i \cdot h$ is not explicitly determined by the state at time $t = (i-1) \cdot h$. This can be seen from the fundamental approximations presented in Eqn (4.9) and Eqn (4.10).

In the current investigation, α and β were chosen as $\frac{1}{2}$ and $\frac{1}{4}$, respectively, in accordance with Eqn (4.19) and Eqn (4.20). For these parameter values, the general Newmark method is referred to as the *constant average acceleration method*. The constant average acceleration method is stable for all time steps h [20]. The size of the interval h was therefore governed only by the need for computational accuracy.

For a given excitation frequency, the parameter N in Table (4.2) determined the size of h . N should be large enough for solution accuracy but small enough to avoid wasted computation time. To determine the appropriate value of N , a convergence analysis was performed.

Figure (4.4) shows the results of the convergence analysis with N . In this analysis, the model's geometry was defined as in Table (3.1). The material matrices \mathbf{M} and \mathbf{K}_{inc} and the dynamic force vector $\mathbf{F}(t)$ were defined as in Table (4.1), with $E=20\text{kPa}$ and $freq=200\text{Hz}$. The forcing function $F_o(t)$ was applied in the negative z -direction at the geometrically central node with coordinates (20,20,20)mm. Figure (4.5) provides an illustration of the loaded model for a 2D “slice” at $x=20\text{mm}$. Figure (4.6) provides an illustration of the forcing function $F_o(t)$ as defined by Eqn (4.6) and the parameters in Table (4.1). As stated earlier, α and β equaled $\frac{1}{2}$ and $\frac{1}{4}$, respectively. PER in Table (4.2) was set to five as the benchmark.

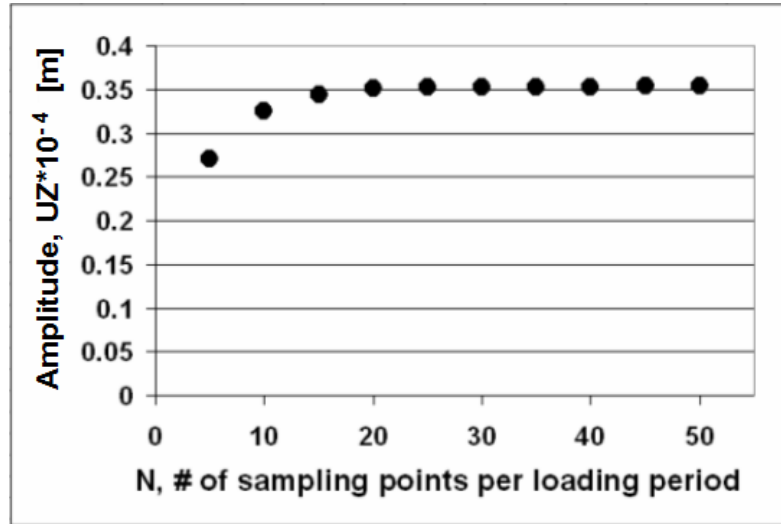


Figure 4.4

Convergence analysis with N sampling points per loading period. The amplitude of the displacement at a particular point in time was plotted as a function of N to help define the appropriate time step h for the Newmark method.

In Figure (4.4), the amplitude of the z -displacement at the loading point (“UZ”) after five excitation periods ($PER=5$) is plotted versus N (the number of sampling points per loading period). The figure shows that after five excitation periods, the solution UZ converges for $N=25-30$. Any larger value of N did not markedly affect the solution. Thus, N was set to 30 for all subsequent analyses.

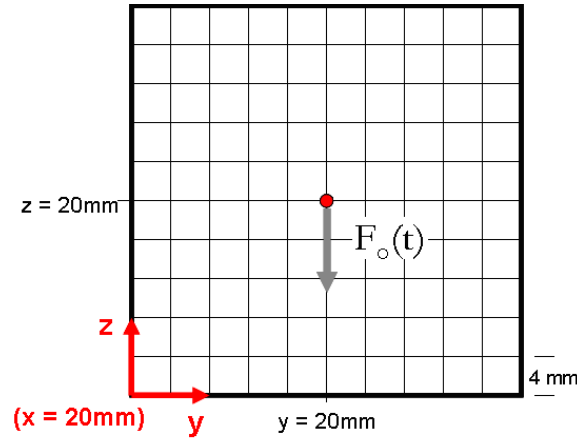


Figure 4.5

A 2D slice of the finite element model with the forcing function $F_o(t)$ applied to the geometrically central node with coordinates (20,20,20)mm. $F_o(t)$ acts in the negative z -direction towards the fixed surface at $z = 0$.

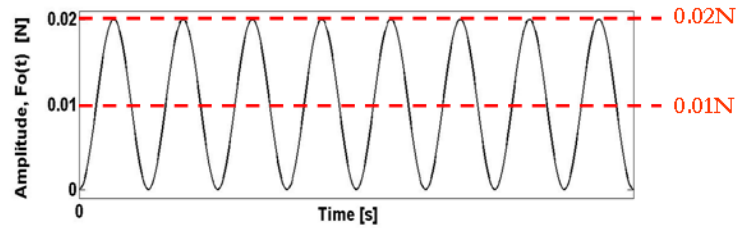


Figure 4.6

The forcing function $F_o(t)$ applied to the model is a harmonic force that is zero at time $t = 0$ oscillating about a mean of 0.01N with an amplitude of 0.01N. The values of the nonzero mean and amplitude were determined using parameters appropriately defined in Table (4.1) from references [5,8,12,13,18,19].

The parameter PER was also investigated; it determined the length of the dynamic analysis (see Table (4.2)). PER must have been sufficiently large to obtain a representative sample of the dynamic solution, yet small to keep computation time in check. Thus, a convergence analysis was performed exactly as described for N , except that N was set equal to 30 and PER was under investigation.

Figure (4.7) shows the results of the convergence analysis with *PER*. ‘UZ’ once again represents the amplitude of the z-displacement at the loading point, now as a function of *PER*. The value of *PER* where the solution converged was not very clear, so an approximate value of *PER* =75 was chosen. Any larger value of *PER* did not markedly affect the solution. Thus, *PER* was set to 75 for all subsequent analyses.

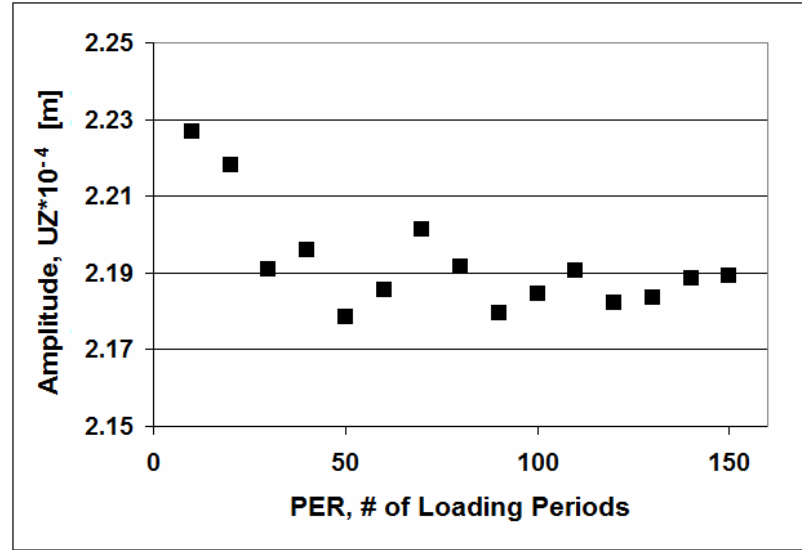


Figure 4.7

Convergence analysis with *PER* loading periods. The amplitude of the displacement with $N=30$ samples per loading period was plotted as a function of *PER* to help determine a sufficient length of time t required for dynamic analysis with the Newmark method.

Although a converged solution for UZ at point (20,20,20)mm was obtained with *PER* =75, it was not known if that particular value was accurate. Since the “true” value was unknown, an error estimate was a seemingly impossible issue to consider. However, external methods were used to affirm the solution computed here; these “external methods” included a transient dynamic analysis with ANSYS 10.0 and a “short-cut” method to solve the equations of motion using assumptions valid only for harmonic motion imaging. The results from these methods are discussed in Section 4.2.3 and Section 5.3, respectively.

4.2.2 Starting Conditions

When $i = 0$, the vectors \mathbf{D}_i , $\dot{\mathbf{D}}_i$, and $\ddot{\mathbf{D}}_i$ contained the starting conditions of nodal displacement, velocity, and acceleration, respectively, in the Newmark method. To solve for $\mathbf{D}(t)$, these vectors were specified at the start of the analysis for the first iteration at $i = 1$ (recall that $\mathbf{D}_1 = \mathbf{D}_1(\mathbf{D}_0, \dot{\mathbf{D}}_0, \ddot{\mathbf{D}}_0, \mathbf{F}_1)$). In this investigation, it was assumed that

$$\begin{bmatrix} \mathbf{D}_0 \\ \dot{\mathbf{D}}_0 \\ \ddot{\mathbf{D}}_0 \end{bmatrix} = \mathbf{0}. \quad (4.21)$$

It was deemed reasonable to assume that the body started from rest because the forcing function $F_o(t)$ equaled zero at time $t = 0$ due to a phase shift of $-\pi/2$ (see Eqn (4.6) for $F_o(t)$).

4.2.3 Programming Assessment

A transient dynamic analysis was performed in ANSYS 10.0 to assess the validity of the current MATLAB simulation. In ANSYS, transient dynamic analyses are used to determine the dynamic response of structures under the action of any general time-dependent loads. The ANSYS program uses the Newmark method to solve the equations of motion in Eqn (4.1).

The parameters used to set up a transient dynamic analysis in ANSYS on the current soft tissue model are listed in Table (4.3). With the exception of ‘ELEMENT TYPE’ and ‘NU’, the properties of Table (3.2) were used to construct the model’s geometry and boundary conditions. The SOLID185 element with mixed u/p formulation was used to construct \mathbf{K}_{inc} (see Section 3.2.1). Poisson’s ratio ‘NU’ was set to 0.495 in accordance with Table (4.1). The complete instructions for performing this analysis in ANSYS are included in the Appendix.

ANSYS Parameter	Value/ Specification	MATLAB Equivalents	
		Parameter	(Table)/[Section] reference
DENSITY	1100	ρ	(4.1)
E	20000	E	(4.1)
NU	0.495	ν	(4.1)
SCALAR PARAMETERS:	-	-	-
FREQ	200	$freq$	(4.1)
T	1/FREQ	T	(4.2)
N	30	N	(4.2)
ANALYSIS TYPE	TRANSIENT	Newmark method	[4.2]
MASS	LUMPED	M	[4.1.1]
SOLUTION CONTROLS:	-	-	-
ALPHA	0.25	β	(4.2)
DELTA	0.5	α	(4.2)
VARIABLE 'TIME'	-	$0:h:t$	(4.2)
TIME AT END OF LOAD STEP	0.375	t	(4.2)
TIME STEP SIZE	T/N	h	(4.2)
FUNCTION 'FORCE'	$F + F*\sin(W*\{TIME\} - \{PI\}/2)$	$Fo(t)$	[4.1.2]
F	-0.01	f_o	[4.1.2] & [4.1.3]
W	1256.637061	ω	[4.1.2]

Table 4.3

Parameters used to set up a transient dynamic analysis in ANSYS, which was used to assess the performance of the dynamic analysis performed with the current MATLAB simulation using the Newmark method.

As can be seen from Table (4.3), the transient dynamic analysis set up in ANSYS was defined from the parameters used in the current MATLAB simulation (see the referenced Tables and Sections). The forcing function 'FORCE' was applied in the z-direction at the geometrically central node with coordinates (20,20,20)mm. The magnitude 'F' was made negative so that 'FORCE' was applied towards the fixed surface at $z = 0$, just as was done in the convergence analyses with N and PER in Section 4.2.1. All initial conditions were equal to zero (by default) in accordance with Section 4.2.2.

The z-displacement at the point of loading ('UZ') determined from both MATLAB and ANSYS simulations is depicted in Figure (4.8). UZ from the MATLAB simulation was obtained by

solving Eqn (4.16) at each iteration i in time using the `inv(.)` command in MATLAB to invert $\overline{\mathbf{K}}$.

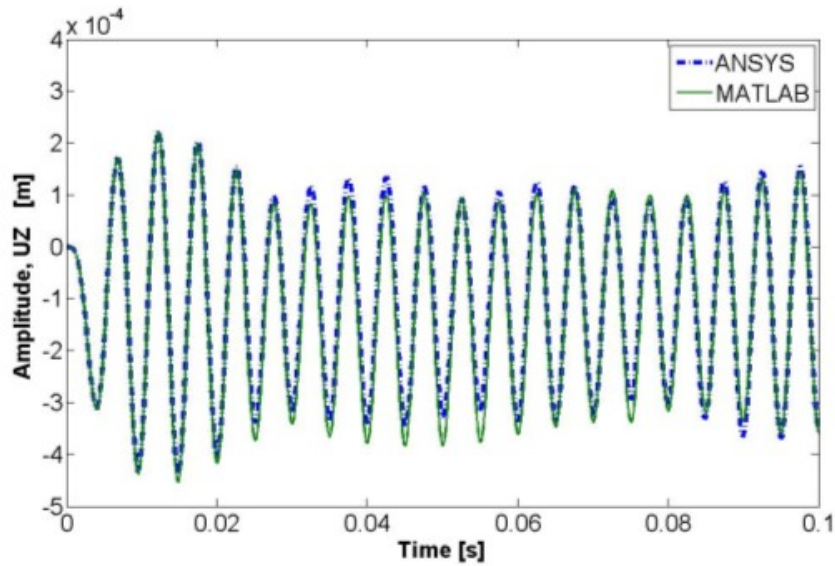


Figure 4.8

The dynamic z-displacement ('UZ') recorded at the point of loading from both MATLAB (—) and ANSYS (--- · ---) simulations.

From Figure (4.8), it was seen that the ANSYS and MATLAB simulations were in good agreement. Any deviations from one simulation to the other were viewed as negligible and were not explored further. It was thus concluded that the dynamic MATLAB simulation was programmed properly because its results were in accordance with a commercial finite element package using the Newmark method, too.

Chapter 5

Dynamic Analysis Results

5.1 Physical Observations

The results obtained in this investigation needed to agree with what has been observed by others to prove that the current analysis was a suitable simulation of soft tissue behavior. This was the main goal of all work discussed up to this point. The next two subsections assess whether or not this goal was achieved.

5.1.1 Massless System Response

A massless elastic system, like the simple spring in Figure (5.1), responds instantaneously to applied force. This occurrence makes physical sense, and should be true for the current simulation if the mass matrix \mathbf{M} is neglected. In this case, the equations of motion for the current soft tissue model would then become

$$\mathbf{K}_{inc} \mathbf{D}(t) = \mathbf{F}(t). \quad (5.1)$$

The displacement at the loading point recorded from the vector $\mathbf{D}(t)$ should be exactly in phase with the forcing function applied to that point, regardless of spring constant, k (or in the case of the current model, Young's modulus, E). Figure (5.2) illustrates the results of such a simulation, with the forcing function $F_o(t)$ from Eqn (4.6) applied in the negative z -direction at point (20,20,20)mm.

The graph in Figure (5.2) shows that the forcing function ($F_o(t)$) and the displacement signal (UZ) measured for several Young's modulus values were out of phase. However, the

displacement signals for each Young's modulus were aligned. This apparent time shift was a side effect of the Newmark method and the choice of starting conditions.

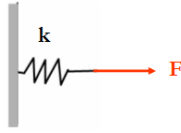


Figure 5.1

A one-dimensional massless elastic system, represented by a simple elastic spring with spring constant k . This figure helps visualize that if the mass in the current finite element simulation was neglected, the model would respond instantaneously to applied force regardless of material stiffness.

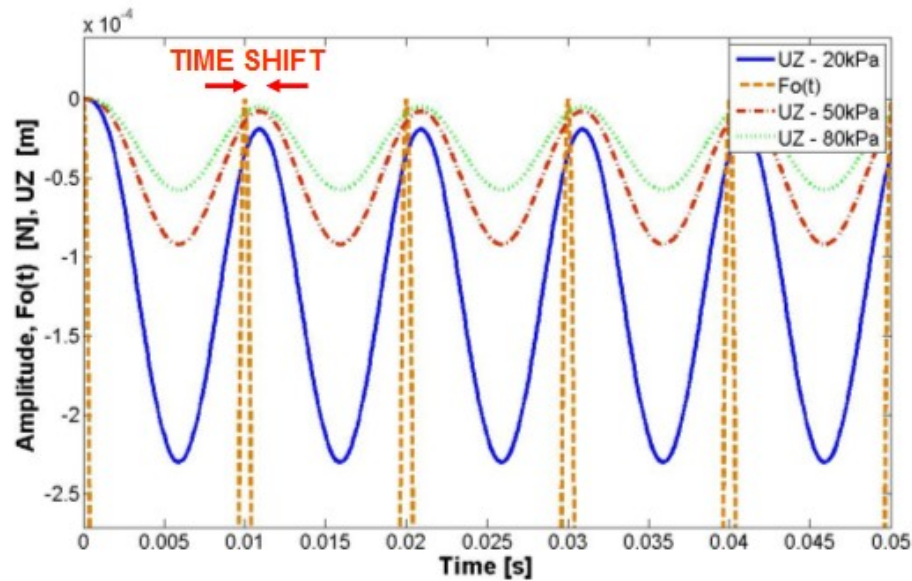


Figure 5.2

The dynamic z-displacement ('UZ') recorded at the point of loading in the current MATLAB simulation for the (massless) tissue model. Three different cases of material stiffness are shown, where Young's modulus E equals 20kPa (—), 50kPa (---), and 80kPa (.....). The forcing function $F_o(t)$ (---) is also depicted. A time shift is also labeled between the displacement responses and the forcing function $F_o(t)$.

The Newmark method, recall, is an iterative procedure where each solution in time depends on the previous solution in time. Since all starting conditions were set to zero, the solution took a few iterations to initially progress. This time shift could complicate future analyses for a viscoelastic system, where phase shift will be considered. In this investigation, though, this time

shift does not affect the amplitude of the displacement, which is the only parameter of the response signal that is of interest for the current elastic system.

5.1.2 Effect of Young's Modulus

The dynamic response of the current soft tissue model governed by the equations of motion Eqn (5.2) is depicted in Figure (5.3).

$$\mathbf{M}\ddot{\mathbf{D}}(t) + \mathbf{K}_{inc}\mathbf{D}(t) = \mathbf{F}(t) \quad (5.2)$$

The forcing function $F_o(t)$ in the vector $\mathbf{F}(t)$ was applied in the negative z -direction of the geometrically central node. The z -displacement at that point (UZ) was recorded for two different Young's modulus values and is shown in the figure. As discussed in the previous section, an inherent time shift will be present in all solutions computed with the Newmark method.

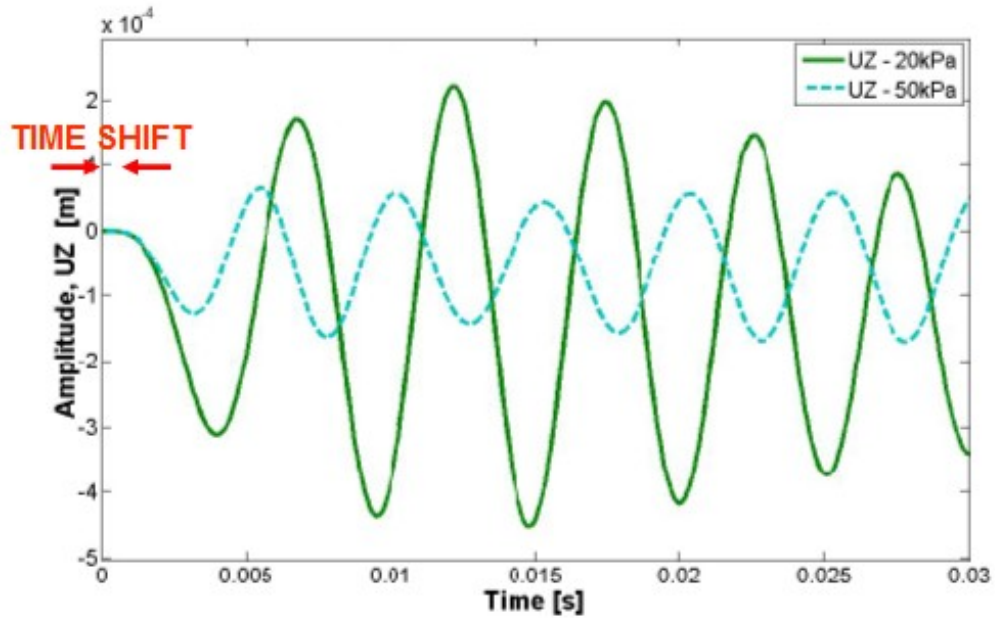


Figure 5.3

Dynamic response of the current tissue model (with mass). Two different cases of material stiffness are shown, where Young's modulus E equals 20kPa (—) and 50kPa (---). The initial time shift introduced by the Newmark method/ starting conditions is also labeled.

From Figure (5.3), it was observed that Young's modulus affects the dynamic solution in two ways. First, as Young's modulus increased, displacement amplitude decreased. This result was intuitive; stiffer materials deform less than softer materials under the same load. This change in displacement amplitude with material stiffness is represented in Figure (5.4) for Young's modulus values ranging from 20 – 60 kPa. The decrease in displacement amplitude with material stiffness/ Young's modulus shown in Figure (5.4) was also observed by Konofagou and Hynynen [8] in their simulations and phantom experiments with harmonic motion imaging (see Section 1.4).

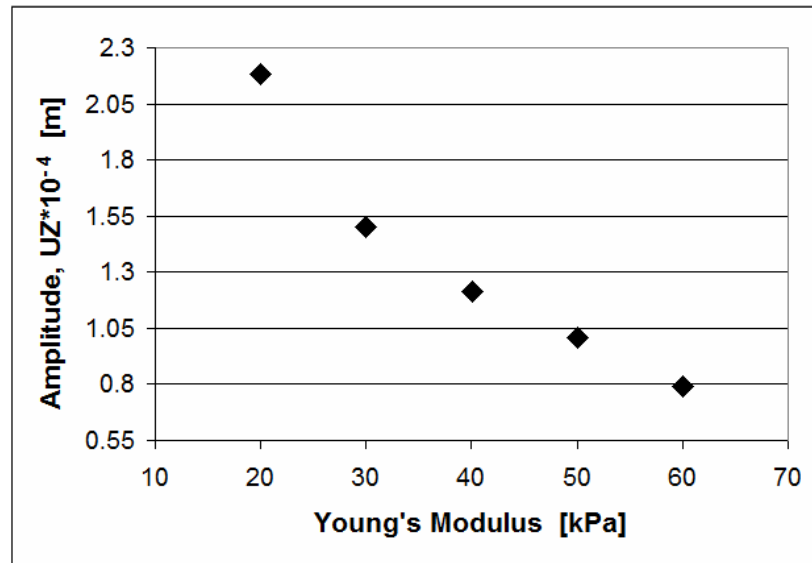


Figure 5.4

A plot of displacement amplitude versus Young's modulus, with values ranging between 20 – 60kPa. Displacement amplitude decreases with material stiffness.

For the current simulation, it was also apparent from Figure (5.3) that the displacement solutions for different Young's modulus values were out of phase; the 50kPa displacement response was shifted ahead of the 20kPa response. Both responses were of approximately the same frequency ($freq = 200\text{Hz}$), so this directly contrasted what was observed for the massless system (see Figure (5.2)). This phase shift between solutions was caused by the initial response time of the material (not to be confused with the initial time shift introduced by the Newmark method/starting

conditions). As Young's modulus increased, the material “caught on” quicker, i.e., the response time decreased. This could be the source of the small apparent upshift in frequency with increasing material stiffness observed by Konofagou and Hynynen [8] (see Section 1.4).

This result can be more easily understood with the one-dimensional mass-spring system shown in Figure (5.5). From the figure, it can be visualized that the mass attached to a stiffer spring will respond more readily to external perturbation than the mass on a softer spring. Likewise, the same is true for the current soft tissue model; if the “springs” are stiffened (i.e., Young's modulus is increased), the lumped mass at the loaded node will respond more quickly to the forcing function, $F_o(t)$. This was just what was observed in Figure (5.3). Thus, in addition to agreeing with experimental findings, the results from the current simulation make physical sense, too. Accordingly, it was concluded that the current finite element analysis was a suitable simulation of soft tissue behavior.

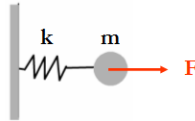


Figure 5.5

A one-dimensional elastic system, shown as a simple elastic spring with a mass on the end. This figure helps visualize that if the material of the current soft tissue model was made stiffer (i.e., the Young's modulus was increased), the material would respond quicker to applied load. This decrease in response time would be evident in the displacement response.

5.2 Multi-Frequency Forcing Function

In previous discussion, the forcing function $F_o(t)$ was comprised of a single excitation frequency, $freq$ (see Section 4.1.2). Figures (5.6) and (5.7) below illustrate the results of two MATLAB simulations obeying this approach. In the two subsequent figures, $F_o(t)$ was applied

to the model at the geometrically central node with coordinates (20,20,20)mm in the negative z -direction. The z -displacement at the point of loading was recorded in time.

$freq$ equaled 100Hz and 200Hz in Figure (5.6) and Figure (5.7), respectively. Young's modulus E equaled 20kPa in both simulations. The force signal and displacement result ('UZ') are the top and middle graphs, respectively, in Figures (5.6) and (5.7). The bottom graph in each figure shows the frequency spectrum of the displacement result. The 'fft' function in MATLAB was used to generate the frequency spectrum.

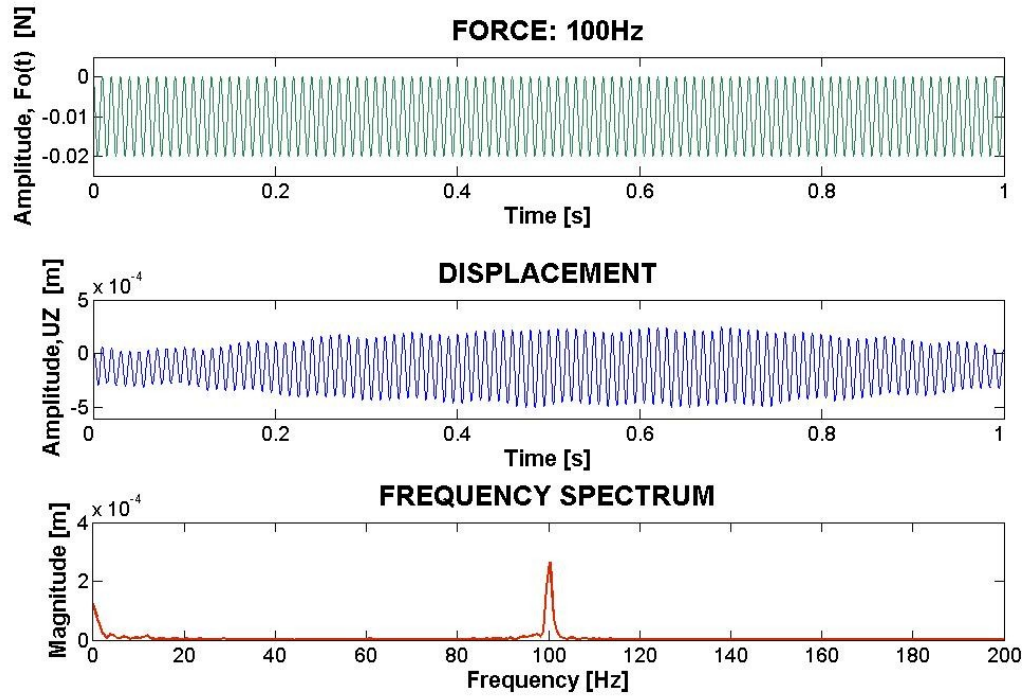


Figure 5.6

100Hz excitation frequency case. $F_o(t)$, as it was applied in the (negative) z -direction at the point of loading is shown in the top graph, and the resulting z -displacement at that point is shown in the second graph. The bottom graph displays the frequency spectrum of the displacement response.

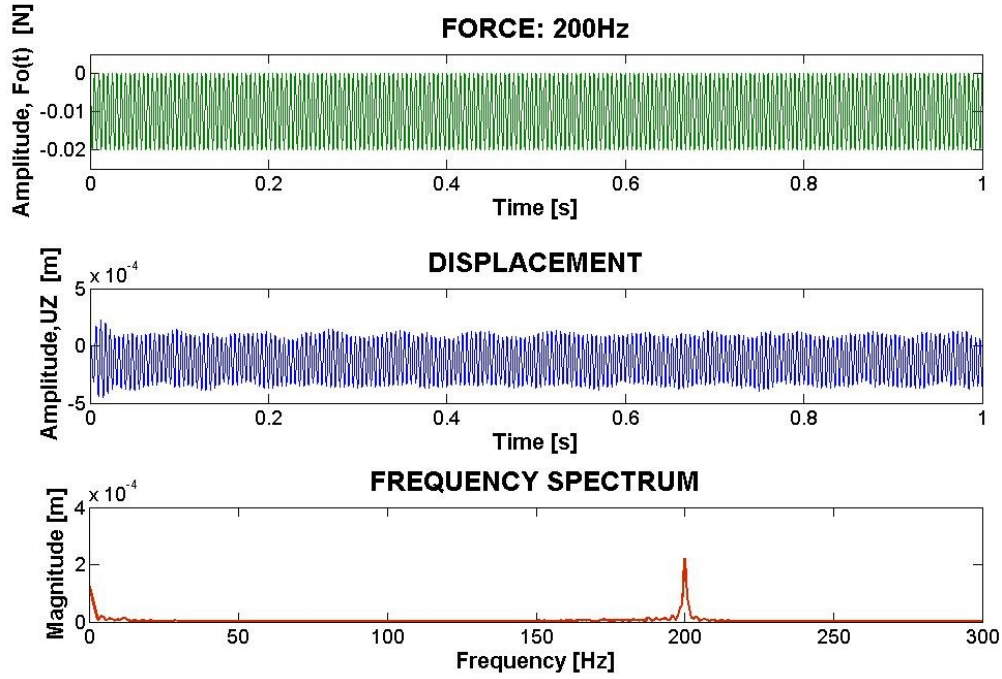


Figure 5.7
200Hz excitation frequency case. Reference the caption of Figure (5.6) for a more thorough description.

As quoted from Section 4.2, the Newmark method “is a popular technique used by engineers to determine the dynamic response of a structure under the action of any general time-dependent load”. So, to utilize the generality of the Newmark method, a forcing function was created with several frequency components, defined as

$$F_o(t) = \sum_{i=1}^4 f_o^i + f_o^i \sin\left(\omega_i t - \frac{\pi}{2}\right) \quad (5.3)$$

where $\omega_i = 2\pi \cdot freq_i$, with $freq_i$ equal 50, 100, 200, and 400Hz, respectively, as per Table (4.1). f_o^i equal 0.01N for each $freq_i$ (see Section 4.1.3). Note that $F_o(t)$ still equals zero at time $t=0$; the assumption of zero starting conditions still applies. Time step h and analysis time t (see Table (4.2)) depend upon $freq$ and were redefined for $F_o(t)$ in Eqn (5.3). T in h was defined for the largest frequency component (400Hz), while the T in t was defined for the smallest frequency

component (50Hz). This provided the smallest time step and longest simulation time necessary in accordance with the convergence analyses discussed in Section 4.2.1.

The results for the forcing function defined by Eqn (5.3) are illustrated in Figure (5.8).

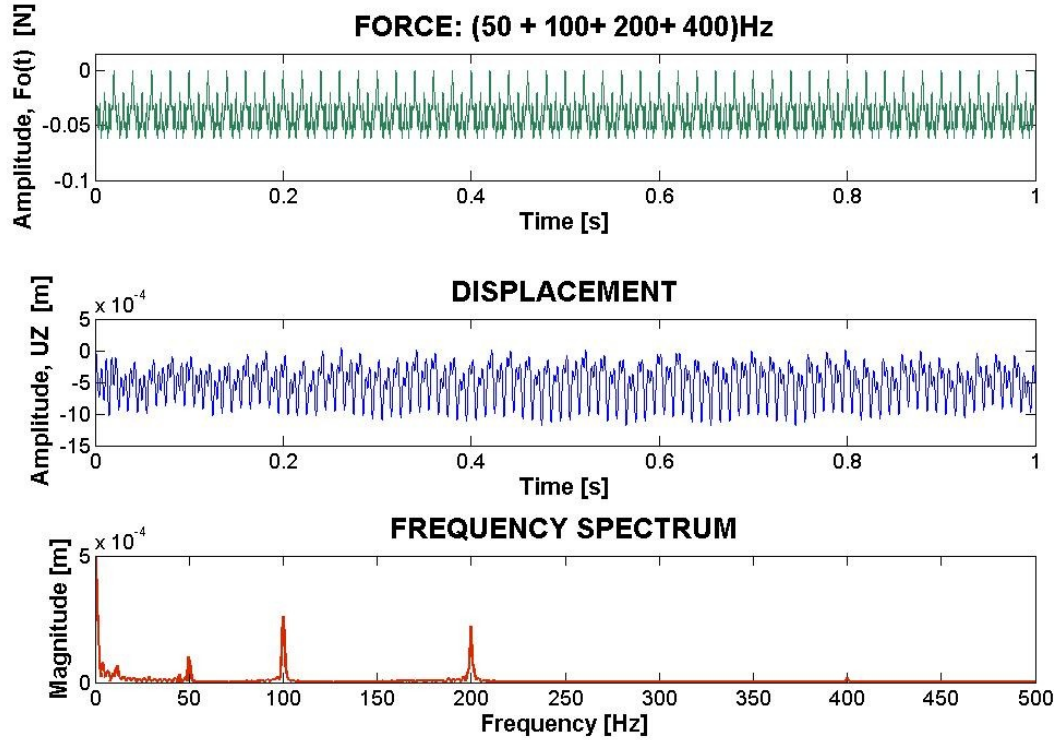


Figure 5.8

Case where the forcing function $F_o(t)$ was composed of four frequency components; 50, 100, 200, and 400Hz. Reference the caption of Figure (5.6) for a more thorough description.

It was surmised that the amplitude of the displacement signal at each excitation frequency in Figure (5.8) equaled the amplitude of the displacement for each single-frequency case. Table (5.1) shows the results of the analysis investigating this claim.

Frequency of Interest (Hz)	Displacement Amplitude [m]				
	Frequency [Hz]				
	50+100+200+400	50	100	200	400
50	1.577E-04	1.590E-04	-	-	-
100	1.521E-04	-	1.549E-04	-	-
200	2.252E-04	-	-	2.184E-04	-
400	1.734E-05	-	-	-	1.739E-05

Table 5.1

Multi-frequency force versus single-frequency force results. Each force case is in a separate column, and the displacement amplitudes for each particular frequency of interest are compared. This was done to assess the efficacy of the Newmark method in handling more than one frequency component in its excitation force.

The displacement amplitudes from single-frequency and multi-frequency forcing functions, with each case labeled in a particular column, are tabulated in Table (5.1). The “Frequency of Interest” indicates the frequency whose magnitude was sought in the displacement response. Thus, the column “50+100+200+400”, indicating the multi-frequency forcing function, contains amplitudes at all frequencies of interest. All amplitude values were obtained from the displacement signals at each frequency of interest using a discrete Fourier transform algorithm devised by Cai [21]. All previous and subsequent displacement amplitudes at a particular excitation frequency were obtained using this algorithm.

While the displacement amplitudes for the multi- and single-frequency forcing functions were proximate, they were not identical. This was because h (time step) and t (analysis time) for each frequency component in the multi-frequency case were not identical to their single-frequency counterparts; h and t in the multi-frequency case had a mixed definition, dependent upon 400Hz and 50Hz, respectively. This observation implies that the convergence analyses performed for N and PER were not an end-all to discussion.

In the multi-frequency case, h and t were taken as the smallest and longest necessary based on the convergence analyses for N and PER , respectively. For the 50, 100, and 200Hz components, the time step h did not need to be 8.3E-5sec (defined from Table (4.2) with $freq = 400\text{Hz}$), while for the 100, 200, and 400Hz components, t did not need to be 1.5sec (defined from Table (4.2) for $freq = 50\text{Hz}$). But apparently, these excessive values of h and t still affected the solution, despite the purpose of the convergence analyses.

5.3 Short-cut Method

The amplitude of the displacement at a given loading point can be obtained without using the Newmark method. If certain assumptions are made about the form of the forcing function and the resulting displacement, the amplitude of the displacement at the point of loading can be determined directly from the equations of motion. Time-history simulation data need not be generated, so this method is referred to as the “short-cut” method. This method was employed as a rough estimate of the accuracy of the Newmark method. The short-cut method described hereafter requires several assumptions and is valid only for harmonic motion imaging (described in Section 1.3).

Let a forcing function $f(t)$ be applied to a point in the model. $f(t)$ has an amplitude of the form

$$f(t) = f \sin \omega t. \quad (5.4)$$

It is reasonable to assume that the resulting displacement at the point of loading will be of the same general form as the forcing function. Additionally, for an elastic system, it can be further assumed that the steady-state displacement response is in phase with the forcing function. Thus, the displacement would take the form

$$u(t) = \sum_j u_o^j \sin \omega^j t. \quad (5.5)$$

The index j indicates that the resulting displacement can be a composition of multiple frequency (ω^j) components. If the frequency components other than the loading frequency are ignored (as is done through filtering during HMI experimentation), the displacement takes the more simplified form given by Eqn (5.6).

$$u(t) = u_o \sin \omega t \quad (5.6)$$

The ω 's in Eqns (5.4) and (5.6) refer to the same frequency.

The equations of motion for the whole model can be reduced to a single equation if the displacement in the direction/node of loading is viewed as the *only* nonzero entry in the displacement vector $\mathbf{D}(t)$. This is a major assumption required for the short-cut method. Thus, the system of equations in Eqn (5.2) become

$$M_{i,i} \ddot{u}(t) + K_{i,i} u(t) = f(t), \quad (5.7)$$

where the subscripts i,i refer to the particular row, column entry of the \mathbf{M} and \mathbf{K} matrices corresponding to the row entry of $\mathbf{F}(t)$ that equals the forcing function $f(t)$. If Eqns (5.6) and (5.4) are substituted into Eqn (5.7) for $u(t)$ and $f(t)$, respectively,

$$\left(-\omega^2 M_{i,i} + K_{i,i} \right) u_o = f. \quad (5.8)$$

Thus, using the assumptions of the short-cut method, the amplitude of displacement u_o in the direction/node of loading can be determined from the forcing frequency ω , the entries $M_{i,i}$ and $K_{i,i}$ of the mass and stiffness matrices, respectively, and the forcing amplitude f .

As mentioned earlier, the short-cut method requires several assumptions and is valid for HMI only. However, the results for u_o can be compared to the displacement amplitudes obtained in the current simulation as long as a harmonic forcing function of the same amplitude is used. Table (5.2) shows the results of both the short-cut method and the current simulation using the Newmark method. The displacement amplitudes for various frequencies (ω in Eqn (5.8)/*freq* in

Eqn (4.7)) at various nodes within the model were explored and are included in the table. Figure (5.9) illustrates the location of these nodes in the model; all of these nodes were taken along the z -direction line directly in the center of the model. In Table (5.2), all amplitudes were obtained with $E = 20\text{kPa}$, f (Eqn (5.4)) = f_o (Eqn (4.6)) = 0.01N .

		Frequency [Hz]							
		50		100		200		400	
		Displacement Amplitude [m]							
Coordinates [mm] (x,y,z)	Node #	Newmark	short-cut	Newmark	short-cut	Newmark	short-cut	Newmark	short-cut
(20,20,8)	303	1.097E-04	1.129E-04	1.567E-04	7.420E-04	2.185E-04	2.163E-04	1.839E-05	1.788E-05
(20,20,12)	424	1.248E-04	1.122E-04	1.538E-04	2.329E-05	2.230E-04	2.224E-04	1.856E-05	1.705E-05
(20,20,16)	545	1.404E-04	1.030E-04	1.461E-04	1.807E-04	2.246E-04	2.249E-04	1.821E-05	1.901E-05
(20,20,20)	666	1.577E-04	1.037E-04	1.521E-04	2.003E-04	2.252E-04	2.262E-04	1.734E-05	1.805E-05
(20,20,24)	787	1.762E-04	8.834E-05	1.614E-04	1.054E-04	2.254E-04	2.265E-04	1.670E-05	1.725E-05
(20,20,28)	908	1.925E-04	6.156E-05	1.640E-04	6.852E-04	2.257E-04	2.299E-04	1.685E-05	1.919E-05
(20,20,32)	1029	2.018E-04	3.813E-05	1.737E-04	9.275E-04	2.301E-04	2.360E-04	1.737E-05	1.812E-05
(20,20,36)	1150	2.099E-04	4.204E-05	2.372E-04	2.459E-04	2.332E-04	2.435E-04	1.916E-05	1.948E-05

Table 5.2

A comparison of the short-cut and Newmark methods, where displacement amplitudes are displayed for several nodes and excitation frequencies acquired with both methods. The short-cut method was employed as a rough estimate of the accuracy of the Newmark method.

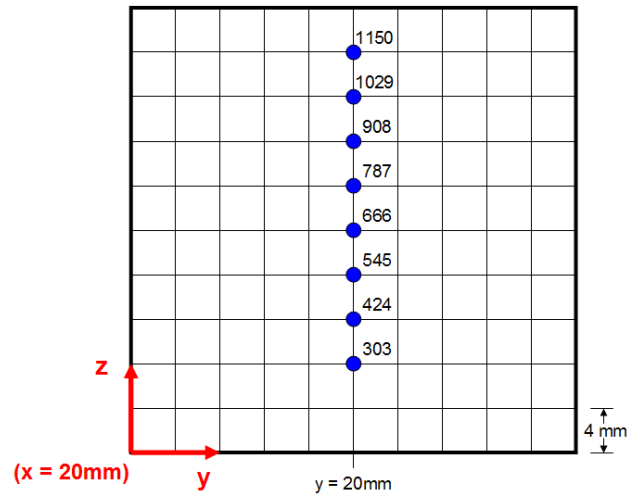


Figure 5.9

A 2D slice of the model indicating the nodes listed in Table (5.2). All nodes lie along the z -direction in the center of the model.

The results from the Newmark method in Table (5.2) were obtained with the multi-frequency forcing function discussed in Section 5.2. Each node in the table was loaded in the negative z -direction, and the resulting z -displacement amplitude was obtained at that node only. Since each node was loaded one at a time, eight separate multi-frequency Newmark analyses were run on eight different points. Since the short-cut method could only handle one frequency at a time, it was run 32 times to address four different frequencies at eight nodes.

From the start of this analysis, it was not expected that the short-cut and Newmark methods would yield identical results. Since the short-cut method required so many assumptions, it was expected that this loss of information would take its toll on the solution. From the results in Table (5.2), one can observe that the short-cut and Newmark methods provided generally agreeable results but deviated greatly in some instances.

The information lost in the short-cut method, contributing to the smaller deviations, were the entries of the displacement vector other than u_o at the node, direction of loading. Before reducing the equations of motion of the current model to Eqn (5.8), each row of the stiffness matrix was multiplied by the displacement vector to determine each entry in the force vector. This was a simple matter of linear algebra.

In the short-cut method, all but one of the multiplications between the stiffness matrix and displacement vector were ignored. Compared to the Newmark method, where no assumptions of that kind were made, it was likely to see discrepancies between amplitude results. If the rest of the displacements in the displacement vector were incorporated into the short-cut method, more agreeable results to that of the Newmark method would have been expected.

The larger deviations between the short-cut method and the Newmark method, apparent for the nodes closest to the free surface, most likely pertain to the frequency response of the model. This is an extremely important consideration that must be addressed in future work. It was not addressed in this investigation because a thorough frequency analysis detracted from the main goal: to develop a dynamic finite element simulation in MATLAB, and to see if its results agreed with those from other methods (i.e., ANSYS and the short-cut method).

On the small scale between 0 to 12kHz, Konofagou et al. [14] observed an unpredictable relationship between displacement amplitude and excitation frequency in their simulations of USAE (see Section 1.4). At node 545, for example, there does not seem to be a trend between displacement amplitude and excitation frequency. The same tendency holds for all the other nodes in Table (5.2). Although the general trend observed by Konofagou et al. [14] was that displacement amplitude decreased with excitation frequency, the range of frequencies tested here was not wide enough to draw the same conclusion, hence contributing to the need for a future frequency analysis.

The short-cut method was deemed acceptable as a quick procedure to get a general idea of the displacements anticipated for the current problem. It helped reinforce the questionable issue of solution accuracy for the current simulation with the Newmark method, a point previously unaddressed.

Chapter 6

The Inverse Problem – A Current Concern

6.1 Methodology

The eventual goal of this research team is to develop a routine to determine the Young's modulus of a given model from its simulation data. In other words, it is hoped that once the displacement data is obtained from the simulation, it can be used to “guess back” the value of the Young's modulus in the stiffness matrix of the model. If the routine can perform this task on the simulation data, it can be applied to experimental data acquired for actual soft tissue.

Recall Eqn (5.8) from the short-cut method, which is repeated below for convenience.

$$\left(-\omega^2 M_{i,i} + K_{i,i}\right) u_o = f$$

This equation was obtained from the system of equations for the current model by assuming that the applied force and the resulting displacement were both harmonic in form and in phase, with magnitudes u_o and f , respectively. It was further assumed that aside from the displacement at the loading point, no other nodes in the model were affected by the applied force. This reduced the equations of motion for the model, a system of equations, to a one degree of freedom system in the direction/ node of loading. Only one frequency component (ω) at a time can be considered (the multi-frequency forcing function discussed in Section 5.2 is not applicable here).

Recall from Section 5.3 that the subscripts i,i refer to the particular row, column entry of the **M** and **K** matrices corresponding to the row entry of **F(t)** that equals the forcing function $f(t)$. Thus,

the value $K_{i,i}$ can be thought of as the stiffness of a small volume of material surrounding the point of loading, and can be determined by

$$K_{i,i} = \frac{f}{u_o} + \omega^2 M_{i,i} . \quad (6.1)$$

Young's modulus can be determined from $K_{i,i}$ because the incompressible stiffness matrix is directly proportional to E . In other words,

$$K_{i,i} = E \cdot C_{i,i} , \quad (6.2)$$

where C is the stiffness matrix \mathbf{K} generated with $E = 1\text{Pa}$.

Before the equations of motion of the current model were reduced to Eqn (5.8), each row of the stiffness matrix was multiplied by the displacement vector to determine each entry in the force vector. Figure (6.1) provides an illustration of this procedure, which is just a matter of linear algebra. This concept was mentioned earlier for the short-cut method discussed in Section 5.3.

$$\begin{bmatrix} K_{1,1} & K_{1,2} & \cdots & K_{1,3630} \\ K_{2,1} & K_{2,2} & \cdots & K_{2,3630} \\ \vdots & \vdots & \ddots & \vdots \\ K_{3630,1} & K_{3630,2} & \cdots & K_{3630,3630} \end{bmatrix} \cdot \begin{bmatrix} u_x^1 \\ u_y^1 \\ \vdots \\ u_z^{1210} \end{bmatrix} = \begin{bmatrix} F_x^1 \\ F_y^1 \\ \vdots \\ F_z^{1210} \end{bmatrix}$$

Figure 6.1

An illustration of the linear algebra employed for the multiplication of the stiffness matrix and the displacement vector to determine each value in the force vector.

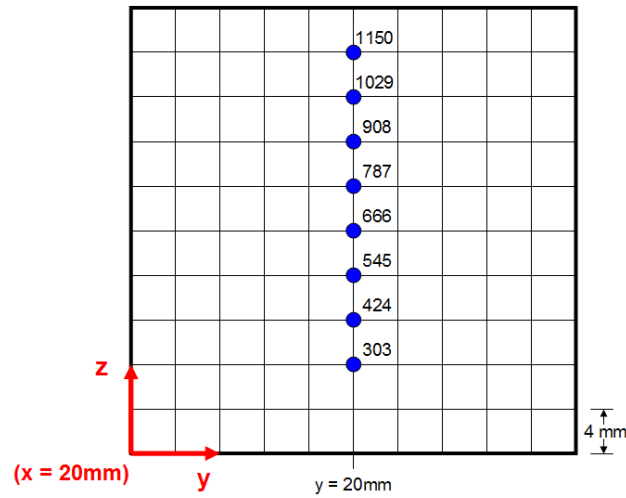
Just as ignoring the rest of the displacement vector in the short-cut method affected the results there, so, too, did it affect the value of $K_{i,i}$ determined by Eqn (6.1). Table (6.1) lists a series of stiffness entries $K_{i,i}$ determined from both the original stiffness matrix \mathbf{K}_{inc} and Eqn (6.1). The nodes listed in Table (6.1) refer to the same nodes in Table (5.2) and Figure (5.9). Figure (5.9) is included below Table (6.1) for convenience. The row entry of the displacement vector containing

the z -displacement of the node in question is denoted by the subscript i when $K_{i,i}$ is determined from \mathbf{K}_{inc} . In Eqn (6.1), u_o for $K_{i,i}$ was taken from the Newmark method results in Table (5.2) for 200Hz.

Node #	$K_{i,i}$	
	\mathbf{K}_{inc}	Eqn (6.1)
303	1412.6	158.2
424	1412.6	157.3
545	1412.6	156.8
666	1412.6	156.7
787	1412.6	156.6
908	1412.6	156.7
1029	1412.6	155.3
1150	1412.6	155.2

Table 6.1

A comparison of the stiffness matrix entries collected from the original stiffness matrix versus that computed from the short-cut method (Eqn (6.1)).



In Table (6.1), $K_{i,i}$ from \mathbf{K}_{inc} for all the nodes are all identical; this is expected because they are all interior nodes in a homogeneous medium. The same is generally true with $K_{i,i}$ computed from Eqn (6.1). Note, though, that $K_{i,i}$ from Eqn (6.1) is much smaller than $K_{i,i}$ from \mathbf{K}_{inc} ; this is the effect of neglecting virtually the entire displacement vector, as discussed in Section 5.3 and earlier in this section.

To increase the accuracy of $K_{i,i}$ from Eqn (6.1), more entries in the displacement vector need to be considered. Recall that the displacements listed in Table (5.2) for nodes 303 – 1150 are for eight different equilibrium configurations of the equations of motion; they cannot be compiled into a single displacement vector. As currently implemented, HMI does not monitor the displacement at points other than the one under loading. Thus, if adhering strictly to the protocol of HMI, the accuracy of $K_{i,i}$ from Eqn (6.1) cannot be improved; the analysis is bounded by the obtainable data. This suggests that a deviation from the protocol of HMI is necessary for the proposed inverse routine.

6.2 Principle of Superposition

In a single equilibrium configuration, the principle of superposition can be used to determine the displacement at nodes adjacent to the node being loaded, which can then be used to fill in missing values of the displacement vector. This principle is illustrated for the pair of nodes 424 and 303 in Figure (6.2). Note that the entire displacement vector in a given equilibrium configuration is obtainable in the current computer simulation, but to no avail; the experimental protocol of HMI is adhered to as much as possible.

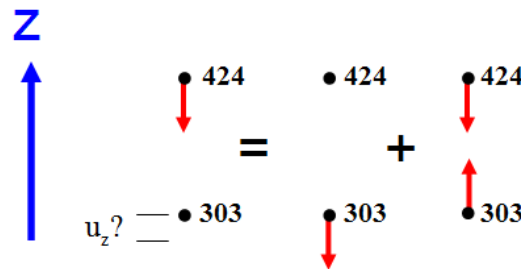


Figure 6.2

An illustration of the principle of superposition, used in the proposed inverse routine. This principle helps determine the displacement at nodes adjacent to the one under loading in a single equilibrium configuration.

In Figure (6.2), the red arrows indicate the direction of force application in each node arrangement, which represent three separate equilibrium configurations with three different force

vectors (see Figure (4.3) for HMI). In terms of nodes 424 and 303, the question in Figure (6.2) asks, “What is the z -displacement at node 303 if node 424 is loaded in the z -direction?”. The answer to this question will be hereby denoted as ‘ $u_z 303(424)$ ’. This is the question posed by the first node arrangement (to the left of the equal sign).

The answer to this question lies in two separate equilibrium configurations (one of which is possible with HMI). The first node arrangement to the left of the equal sign denotes $u_z 303(303)$, or in other words, the z -displacement at node 303 as a result of z -direction loading at node 303. $u_z 303(303)$ can be obtained with HMI. The second node arrangement to the left of the equal sign denotes $u_z 303(424-303)$, denoting the z -displacement at node 303 computed from the configuration where both node 424 and node 303 are loaded such that the space between them is compressed. This configuration is called ‘dipole compression’. This scenario of the principle of superposition is applicable to the other nodes pictured in the illustration below Table (6.1).

To summarize the discussion, the displacements represented by Figure (6.2) are

$$u_z 303(424) = u_z 303(303) + u_z 303(424 - 303). \quad (6.3)$$

The displacement value $u_z 303(424)$, determined through superposition, can be added to the displacement vector in the equilibrium configuration for loading at node 424.

In Figure (6.2), the principle of superposition was used to determine the displacement at the adjacent node *below* the node of loading. Figure (6.3) illustrates the principle of superposition, but for the case when the adjacent node is *above* the node of loading.

The discussion for Figure (6.3) is similar to that of Figure (6.2), and is represented by Eqn (6.4).

$$u_z 545(424) = u_z 545(545) + u_z 545(545 - 424). \quad (6.4)$$

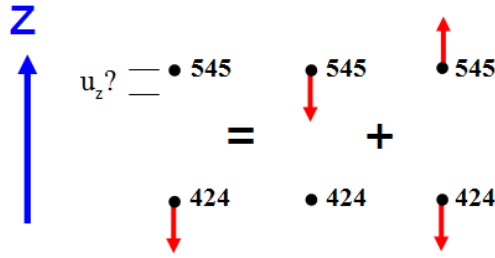


Figure 6.3

An illustration of the principle of superposition, used in the proposed inverse routine. As opposed to Figure (6.2), the adjacent node of interest is now above the node being loaded.

The question in Figure (6.3) asks, “What is the z -displacement at node 545 if node 424 is loaded in the z -direction?”. The answer to this question is denoted as ‘ $u_{z545}(424)$ ’ in Eqn (6.4). Similar to the previous case in Figure (6.2), the answer to this question lies in two separate equilibrium configurations (one of which is possible with HMI). The first node arrangement to the left of the equal sign denotes $u_{z545}(545)$, or in other words, the z -displacement at node 545 as a result of z -direction loading at node 545. $u_{z545}(545)$ can be obtained with HMI. The second node arrangement to the left of the equal sign denotes $u_{z545}(545-424)$, denoting the z -displacement at node 545 computed from the configuration where both node 545 and node 424 are loaded such that the space between them is elongated. This configuration is called ‘dipole tension’. This scenario of the principle of superposition is applicable to the other nodes pictured in the illustration below Table (6.1).

6.3 Proposed Routine

Previously, when adhering strictly to the protocol of HMI, if only the z -direction of node 424 was loaded, as illustrated in Figure (6.4), only one entry in the displacement vector was considered ($u_{z424}(424)$ in Figure (6.4)). However, the principle of superposition described in the previous section adds two more values to the displacement vector ($u_{z303}(424)$ and $u_{z545}(424)$ in Figure (6.4)). Note that these u_z values are the amplitude of displacement; there were taken from the

dynamic response at the frequency of excitation to effectively create static values of $\mathbf{F}(t)$ and $\mathbf{D}(t)$ for the inverse routine.

$$\mathbf{F} = \begin{bmatrix} 0 \\ \vdots \\ f_z^{424} \\ \vdots \\ 0 \end{bmatrix} \longrightarrow \mathbf{D} = \begin{bmatrix} 0 \\ \vdots \\ u_z 303(424) \\ \vdots \\ u_z 424(424) \\ \vdots \\ u_z 545(424) \\ \vdots \\ 0 \end{bmatrix}$$

Figure 6.4

An illustration of the force and displacement vectors for a given equilibrium configuration of HMI with two additional values filled in by using the principle of superposition.

After the first approximation of $K_{i,i}$ was acquired from Eqn (6.1), the original \mathbf{K}_{inc} could no longer be used to generate subsequent simulation data for the displacement at adjacent nodes, because technically, in the inverse routine, nothing is known about the stiffness matrix for the model. Thus, $u_z 303(424)$ and $u_z 545(424)$ must be determined using a “new” stiffness matrix \mathbf{K} constructed from $K_{i,i}$. However, the manner of how $K_{i,i}$ should affect this “new” \mathbf{K} is unknown, and is left for future work.

The general procedure of the proposed inverse routine is illustrated in Figure (6.5). First, u_o from Table (5.2) is used in Eqn (6.1) to determine the first approximation of $K_{i,i}$. Next, $K_{i,i}$ can (somehow) be used to define the “new” stiffness matrix \mathbf{K} , which is needed in the following dipole compression/tension configurations. The displacement at the adjacent nodes is determined from the dipole compression/tension configurations using the principle of superposition. These adjacent displacements then help determine $K_{i,i}$ once again (second approximation), which can then be used to determine $u_z 424(424)$ in yet another forward simulation. If $u_z 424(424)$ is close to

u_o (this criteria has not yet been defined), the inverse procedure ends and Young's modulus E can be determined from Eqn (6.2). If not, subsequent iterations must be performed, with $K_{i,i}$ continually being added to the components in the “new” \mathbf{K} matrix.

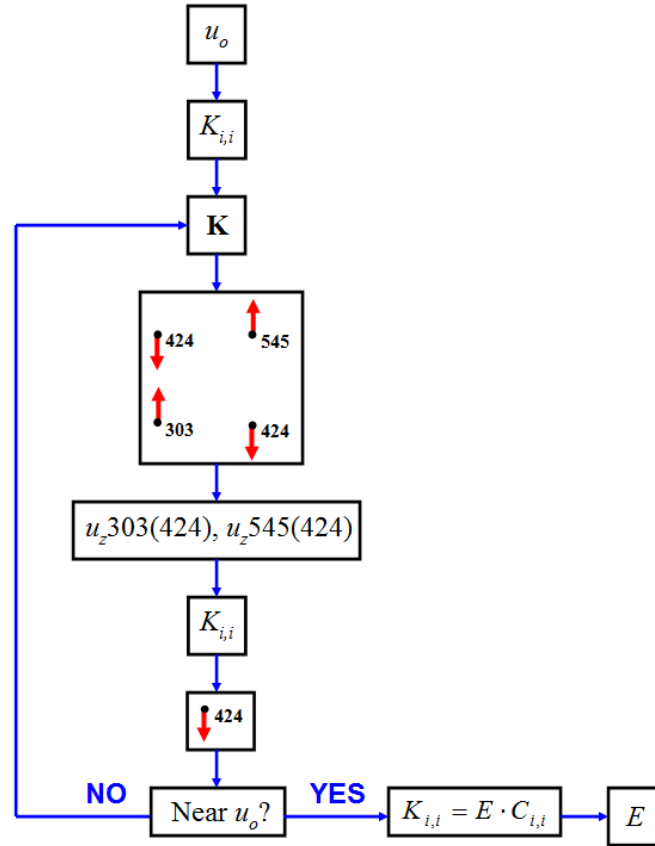


Figure 6.5

The general procedure of the proposed inverse routine.

Chapter 7

Conclusions

This investigation assumed that soft tissue behaved as a linear, isotropic, elastic, incompressible material experiencing small deformations under isothermal loading conditions. These aspects were incorporated into the formulation of the finite element method, which described the current soft tissue model. While these behaviors are generally not observed experimentally, these assumptions greatly facilitated the development of the current simulation; too many variables too soon would have made progress difficult. Many other researchers use these same assumptions when describing soft tissue, so they were regarded as an acceptable starting point for this team's research.

As downloaded from the internet, the original source code was capable of solving the static problem for compressible materials only. To assess the accuracy of the source code, its results for the local stiffness matrix and the static solution were compared to that obtained with a commercial finite element package. Since sufficient agreement was obtained, alterations in the formulation of the local stiffness matrix were employed to address the near incompressibility of soft tissues. These alterations were successfully implemented in the source code, as confirmed by commercial finite element results.

The static analysis with the source code proved the successful creation of an incompressible material model. However, since the goal of this investigation was to simulate the elasticity imaging technique of harmonic motion imaging (HMI), a dynamic finite element analysis needed to be performed. For this, a time-varying forcing function was defined from appropriate

parameters found in the literature. This forcing function mimicked the form of the acoustic radiation force created during HMI experimentation.

With a mass matrix formulated using the lumped mass approach, the finite element equations of motion for the model were constructed. These equations contained the material matrices of mass and stiffness, and the global vectors of nodal accelerations, displacements, and applied force; the current soft tissue model did not incorporate any viscosity effects, hence the absence of a damping matrix. The forcing function was applied to only one node in one direction at any given time, in following with the capabilities of HMI.

To solve the newly defined finite element equations of motion for the current soft tissue model, the Newmark method was applied. This method is an iterative technique commonly used by engineers to determine the dynamic response of a structure under the action of any general time-dependent loads. Starting conditions for the global vectors of nodal accelerations and displacements were necessary to begin the analysis. Convergence analyses were performed to assess the appropriate values of two parameters required for the Newmark method routine; the size of the time step ' h ' and the total time of analysis ' t ', which were defined by the number of samples per loading period (' N ') and the total number of loading periods applied (' PER '), respectively.

The purpose of the convergence analyses was to help define the values required for N and PER to obtain sufficient solution accuracy. These values defined h and t , respectively, for a scenario where the forcing function was composed of one frequency component. For a forcing function with multiple frequency components, it was surmised that if h was defined from N for the highest frequency component and if t was defined from PER for the smallest frequency component, the results from the multi-frequency case would be the same as those obtained from each individual

frequency case. It was found, though, that while the results were proximate, they were not identical. This suggested that h and t needed to be set values, sufficiently small and large, respectively, for any range of excitation frequencies that may be applied. This “for any” definition of h and t would, however, result in a phenomenal waste of computation time over the life of the simulation. The most practical alternative is to define h and t for each single/multi-frequency case that is encountered, as was done in the current investigation.

The current soft tissue model could be thought of as a three-dimensional network of elastic springs with lumps of mass concentrated at each node. If the mass at each node was removed, it was expected that under applied load, the structure’s displacement response would be instantaneous. However, this was not observed; the displacement response for several material stiffness values were in phase with each other but lagged the forcing function for the massless system. This apparent time shift could only be due to the Newmark method and the choice of starting conditions.

The Newmark method is an iterative routine, where each solution in time depends on the previous solution in time. Since the starting conditions were set equal to zero in this investigation, the displacement solution took several iterations to progress from the zero starting value. This time shift was a side effect of the Newmark method, and while it did not affect the current investigation (which was interested only in the displacement amplitude for an elastic material), this time shift could complicate future analyses for viscoelastic systems, where the phase shift between the solution and forcing function must be considered.

When mass was added back to each node in the model, an initial time shift from the Newmark method/starting conditions was still observed. However, it was not known whether this time shift

was the same as that for the massless system. Any future removal of the initial time shift must be carefully considered.

It was also found from the current simulation (with mass) that displacement amplitude decreased with increasing Young's modulus. Furthermore, it was seen that an increase in Young's modulus signified a decrease in response time for the material. This observation was easily visualized with a simple mass-spring system; the stiffer the spring, the more readily the attached mass would respond to applied load. These two observations, which made physical sense and had been observed by others, suggested that the current dynamic analysis was a suitable simulation of soft tissue behavior.

Solving the finite element equations of motion for the current soft tissue model with the Newmark method was the crux of this research. In the end, some final conclusions were drawn about this approach, both positive and negative. The most positive aspect of the Newmark method, and the reason for its selection, is that it can be used with any general time-dependent forcing function. The harmonic forcing function used in the current investigation was a simple one, and did not take full advantage of the method's capabilities. Although more complex forcing functions were not used here, they may be used in the future to learn more about the behavior of soft tissues.

The negative aspects of the Newmark method included the previously discussed time shift introduced into the system. This time shift was due in part to the method itself and also to the choice of starting conditions. The starting conditions could not simply be changed from zero to address this issue, because it was unreasonable to expect that the starting acceleration and displacement at each node in the model are known. This presents another setback to the Newmark method; the fact that starting conditions must be specified in the first place. The last drawback

concerning the Newmark method is that it can get time consuming, depending upon the number of nodes, the step size, and the length of analysis time. As configured in the current investigation, the displacement response for one point using the appropriate values of h and t as defined from the convergence analyses was computed in approximately fifteen minutes. While this does not sound extreme, it must be remembered that this was for a 10x10x10 element model with 1,331 nodes and 3,993 degrees of freedom. Larger models would require some scheme to reduce the size of the problem to make the computation time more manageable.

Chapter 8

Future Work

Soft tissue has generally been observed as anisotropic, nonlinear, and viscoelastic. With elasticity imaging techniques employing focused ultrasound, localized tissue regions can also be ablated as a cancer treatment therapy. The current investigation neglected these observations and proceeded to model the soft tissue as a linear, isotropic material under isothermal loading conditions. To properly design experiments to learn more about the complexities of soft tissue behavior, simulation models play a key role. Thus, a future goal of this team is to incorporate the more complex aspects of soft tissue behavior in the model.

Originally, the viscoelastic features of soft tissue were addressed in a damping matrix included in the finite element equations of motion for the current soft tissue model. This damping matrix was of the appropriate form for a material using the Kelvin-Voigt model of linear viscoelasticity. However, the viscoelastic effects on soft tissue behavior were disregarded in the current investigation when it became apparent that the Newmark method/starting conditions introduced an inherent time shift in the solution response. Analysis of the viscoelastic system required consideration of both the amplitude and phase of the displacement response, and the phase information was tainted by the presence of the time shift. As discussed previously, this time shift may not be the same for all cases (massless, with mass, viscoelastic), so additional research was required before it could be removed. However, the main thrust of the current investigation was to develop a forward finite element analysis on a soft tissue model and to begin some preliminary consideration of the inverse problem. Due to time constraints, it was left as a future consideration.

The frequency response of the model was explored only slightly in the current investigation; only four different excitation frequencies were used to probe the response characteristics of the model. Other researchers have performed full frequency analyses on their models by investigating the amplitude of displacement for a full range of excitation frequencies. The same analysis must be done with the current model to better understand the amplitudes of the displacement, and especially to identify resonant frequencies.

For forward analysis with the current 10x10x10 element model of soft tissue, the computation time was manageable (on the order of fifteen minutes for one loading configuration). However, for larger models, to scan multiple points, computation time could become a real problem. Therefore, it is foreseen that some scheme will be necessary to reduce the size of the problem for practicality's sake. This was attempted in the current investigation by assuming that if a force was applied in the z-direction, the x- and y- displacements as a result of this force would be negligible compared to the z-displacements recorded. Thus, the displacement vector was reduced to every third row (z-displacement entries), and the stiffness matrix was reduced to every third row, third column. However, the displacement amplitudes obtained with this scheme were much smaller than anticipated, suggesting that a more sophisticated reduction scheme is necessary.

The purpose of this investigation was to provide suitable simulation data on soft tissue behavior, so that an inverse routine could eventually be implemented into the current analysis. The inverse routine was only briefly addressed in this research, and was mainly left as a future consideration.

Appendix

ANSYS Directions – Transient Dynamic Analysis

% Define element type

```
PREPROCESSOR>ELEMENT TYPE>ADD
C ADD
C SOLID
C BRICK 8 NODE 185
C OK
C OPTIONS
Pick 'Mixed U/P' in K6 menu (K2 = full integration)
C OK
CLOSE
```

% Define material properties

```
PREPROCESSOR>MATERIAL PROP>MATERIAL MODEL
CC STRUCTURAL
CC LINEAR
CC ELASTIC
CC ISOTROPIC
Set E = 20000, NU = 0.495
CC DENSITY = 1100
OK
MATERIAL>EXIT
```

% Define model geometry

```
PREPROCESSOR>MODELING>CREATE>VOLUMES>BLOCK>BY DIMENSIONS
T 0 0.04 0 0.04 0 0.04 FOR X1, X2, Y1, Y2, Z1, Z2
```

% Define mesh

```
PREPROCESSOR>MESHING>MESH TOOL
C SIZE CONTROLS: GLOBAL SET
C box for NDIV
T 10 FOR NDIV
C OK
C SHAPE: HEX
C MESH
C PICK ALL
C CLOSE
```

```
LIST >NODES
```

* find node with coordinate (0.02, 0.02, 0.02) for force application * (node # 967)

% Define boundary conditions

```
SOLUTION>DEFINE LOADS>APPLY>STRUCTURAL>DISPLACEMENT>ON AREAS
```


C face $z = 0$
 C APPLY
 C ALL DOF
 C on box for VALUES
 T 0 for value of displacement
 C APPLY
 C CLOSE

% Define scalar parameters

UTILITY MENU>PARAMETERS>SCALAR PARAMETERS
 C in selection box
 Enter $FREQ = 200$
 ACCEPT
 Enter $T = 1/FREQ$
 ACCEPT
 Enter $N = 30$
 ACCEPT
 CLOSE

% Set analysis type

SOLUTION>ANALYSIS TYPE>NEW ANALYSIS
 C 'TRANSIENT'
 C 'FULL' FOR SOLUTION METHOD
 C 'YES' FOR LUMPED MASS

% Set analysis options

SOLUTION>ANALYSIS TYPE>SOLN CONTROL
 C transient tab
 Transient effects ON, Stepped load, Newmark algorithm
 Set $ALPHA = 0.25$, $DELTA = 0.5$

% Define TIME variable (Unabridged menu)

SOLUTION>LOAD STEP OPTS>OUTPUT CNTRL>DB/RESULTS FILE
 Item to be controlled: select "nodal DOF solu"
 File write frequency: select "every substep"
 C OK

SOLUTION>LOAD STEP OPTS>TIME/FREQUENC>TIME/TIME STEP
 Time at end of load step: enter 0.375
 Time step size: enter T/N
 Select STEPPED
 Turn AUTOTS, OFF
 C OK

% Define forcing function via Function Editor

SOLUTION>DEFINE LOADS>APPLY>FUNCTIONS>DEFINE/EDIT
 C radians
 $T \text{ 'F + F*sin(W*{TIME} - \{PI\}/2) \text{ (}{\{TIME\}} \text{ appears from pull-down menu)}$
 File>Save
 T 'FORCE' (.func extension)

% Define forcing function as a table parameter via Function Loader

SOLUTION>DEFINE LOADS>APPLY>FUNCTIONS>READ FILE

Define 'table parameter name' & 'constant values'

(' **FORCE**' & F = -0.01, W = $2*\pi*$ FREQ = 1256.637061)

C OK

% Apply load function to node with coordinates (20,20,20)mm

SOLUTION>DEFINE LOADS>APPLY>STRUCTURAL>FORCE>ON NODES

T **967** in blank line on picking menu

C OK

SELECT FZ

Apply as: 'Existing Table' (in drop down)

C APPLY

C OK ('**FORCE**' should be selected)

% Solve

SOLUTION>SOLV CURRENT LS

% Save results

TIME HIST POSTPROC

Close information window

DEFINE VARIABLES

ADD

Select Nodal DOF Result

C OK

T **967** for node number

Enter name: **UZ**

Select Translation Component UZ

C OK

C CLOSE

TIME HIST POSTPROC> LIST VARIABLES

For 1st variable to list: enter **2**

C OK

File>Save As (.txt extension)

CLOSE

References

- [1] American Cancer Society. *Breast Cancer Facts & Figures 2007 – 2008*. Atlanta: American Cancer Society, Inc. 2007.
- [2] American Cancer Society. *Cancer Facts & Figures 2007*. Atlanta: American Cancer Society, Inc. 2007.
- [3] Konofagou E.E., “Quo vadis elasticity imaging?,” *Ultrasonics*, Vol. 42 (1-9), pp. 331-336, 2004.
- [4] Ladeji-Osias, J.O., “The biomechanics of breast palpation: single and multi-probe indentation tests,” Ph.D. Dissertation, Rutgers, The State University of New Jersey, New Brunswick, NJ, 2000.
- [5] Krouskop T.A, Wheeler T.M, Kallel F, Garra B.S, and Hall T., “Elastic moduli of breast and prostate tissues under compression,” *Ultrasonic Imaging*, Vol. 20 (4), pp. 260-274, 1998.
- [6] Wellman P.S, Howe R.D, Dalton E, and Kern K.A., “Breast tissue stiffness in compression is correlated to histological diagnosis,” Technical Report, Harvard BioRobotics Laboratory, pp. 1-15, 1999.
- [7] Egorov V, Tsyuryupa S, Kanilo S, Kogit M, and Sarvazyan A., “Soft tissue elastometer,” *Medical Engineering & Physics*, doi:10.1016/j.medengphy.2007.02.007.
- [8] Konofagou E.E. and Hynynen K., “Localized harmonic motion imaging: theory, simulations and experiments,” *Ultrasound in Medicine & Biology*, Vol. 29 (10), pp. 1405-1413, 2003.
- [9] Maleke C, Luo J, Pelegri A.A, Konofagou E.E., “Mapping of regional tissue mechanical changes using harmonic motion imaging,” *ASME International Mechanical Engineering Congress and Exhibition*, Seattle, WA, 2007, pp.1-7.
- [10] Hynynen K.H. and Konofagou E. U.S. Patent 6 984 209, 2006.
- [11] Maleke C, Pernot M, Konofagou E.E., “Real-time monitoring of regional tissue elasticity during FUS focused ultrasound therapy using harmonic motion imaging,” *International Symposium on Therapeutic Ultrasound*, Boston, MA, 2005, pp. 171-175.
- [12] Maleke C, Pernot M, Konofagou E.E., “A single-element focused transducer method for harmonic motion imaging,” *IEEE Ultrasonics Symposium*, Rotterdam, Netherlands, 2005, pp. 17-20.
- [13] Nightingale K, Soo M.S, Nightingale R, and Trahey G., “Acoustic radiation force impulse imaging: in vivo demonstration of clinical feasibility,” *Ultrasound in Medicine & Biology*, Vol. 28 (2), pp. 227-235, 2002.

- [14] Konofagou E, Thierman J, and Hynynen K., "A focused ultrasound method for simultaneous diagnostic and therapeutic applications – a simulation study," *Physics in Medicine & Biology*, Vol. 46 (11), pp.2967-2984, 2001.
- [15] Liu Y, Kerdok A.E., and Howe R.D., "A nonlinear finite element model of soft tissue indentation," *Lecture Notes in Computer Science – Medical Simulation*, Vol. 3078, pp.67-76, 2004.
- [16] Zaicenco A., "FEM analysis using MATLAB," January 5, 2005.
http://www.geocities.com/anton_6263/fem_mlab.htm?200627 (September 2006).
- [17] Fung Y.C., Biomechanics – Mechanical Properties of Living Tissues, 2nd edition. New York: Springer-Verlag, 1993.
- [18] Palmeri M.L, Frinkley K.D, Oldenburg K.G, and Nightingale K.R., "Characterizing acoustic attenuation of homogeneous media using focused impulsive acoustic radiation force," *Ultrasonic Imaging*, Vol. 28 (2), pp. 114-128, 2006.
- [19] Nightingale K, Nightingale R, Palmeri M, Trahey G., "Finite element analysis of radiation force induced tissue motion with experimental validation," *IEEE Ultrasonics Symposium*, Caesars Tahoe, NV, 1999, pp. 1319-1323.
- [20] Dill E.H., The Finite Element Method for the Mechanics of Solids. Piscataway, NJ: Rutgers University School of Engineering, 2007.
- [21] Cai H., "DFT on a specified frequency," February 4, 2006.
<http://www.mathworks.com/matlabcentral/fileexchange/loadFile.do?objectId=9891&objectType=file> (September 2007).